JGR Space Physics

Key Points:
- Energetic proton data from NOAA POES and EUMETSAT MetOp satellites need further correction and recalibration for long-duration scientific studies
- Compared to rough correction factors regularly used, polynomial functional fits are shown to improve cross calibration
- Differences between the observations and the AP8 model predictions depend on L_m and B/B_0

Correspondence to:
R. Lin,
linrl@nssc.ac.cn

Cross Calibration of >16 MeV Proton Measurements From NOAA POES and EUMETSAT MetOp Satellites

Ruilin Lin[1] , **Jichun Zhang**[2] , **Robert J. Redmon**[3] , **Binbin Ni**[4,5] , **Siqing Liu**[1,6] , **Xiaoxin Zhang**[7] , **Liqin Shi**[1,6], **Jiancun Gong**[8], **Dong Chen**[1], **Yonghong Cheng**[1], **Hong Wang**[9], and **Yong Cao**[9]

[1]National Space Science Center, Chinese Academy of Sciences, Beijing, China, [2]Previously at Space Science Center and Department of Physics, University of New Hampshire, Durham, NH, USA, [3]National Centers for Environmental Information, National Oceanic and Atmospheric Administration, Boulder, CO, USA, [4]Department of Space Physics, School of Electronic Information, Wuhan University, Wuhan, China, [5]CAS Center for Excellence in Comparative Planetology, Hefei, China, [6]University of Chinese Academy of Sciences, Beijing, China, [7]National Center for Space Weather, China Meteorological Administration, Beijing, China, [8]Innovation Academy for Microsatellites, Chinese Academy of Sciences, Shanghai, China, [9]Harbin Institute of Technology Shenzhen Graduate School, Shenzhen, China

Abstract A long-term data set of energetic proton omnidirectional integral fluxes with an 8-s resolution from National Oceanic and Atmospheric Administration (NOAA) Polar Operational Environmental Satellites (POES) and EUMETSAT MetOp satellites from 1978 to 2014 has been investigated comprehensively to capture the data bifurcations, calibration inconsistency, and some erroneous data. There are two categories of the data bifurcations. The upper and lower branches of both bifurcations can be clearly separated by magnetic local time or by magnetic latitude. The calibration inconsistency of POES and MetOp proton omnidirectional integral fluxes (>16 MeV) is solved by fitting the data from each pair of two satellites using a third-degree polynomial function. The fitted curve is almost independent of L_m, B/B_0, and time in the valid range. By these fitted functions, the >16 MeV proton omnidirectional integral fluxes from other POES and MetOp satellites are recalibrated to the NOAA-15 measurements that are adopted as the reference standard. Analyses of the recalibrated data at the geomagnetic equator for about 3.5 solar cycles indicate that the maximal and minimal yearly values of >16 MeV proton omnidirectional integral fluxes are in 1987 and in 2002, respectively. By comparisons with the AP8 model predictions, the ratios of the observations in 1987 (in 2002) to the AP8 MIN (AP8 MAX) predictions are mainly within 0.5-3 (0.1-2), showing a dependence on L_m and B/B_0.

1. Introduction

The proton radiation belt consists principally of energetic protons trapped by the Earth's magnetic field at energies from 100 keV up to several hundred MeV (Miroshnichenko, 2003; Sawyer & Vette, 1976). Its shape looks like a giant doughnut centered over the magnetic equator. For the radiation belt protons with different energies, the inner boundaries of their occupied areas are about several hundred kilometers above the ground, and the outer boundaries are very different. Based on the AP8 model (Sawyer & Vette, 1976), the outer boundaries are confined to $L<3.7$ for trapped protons with $E{\geq}10$ MeV, and beyond geostationary orbit for trapped protons with $E{\leq}1$ MeV. Radiation belt protons originate from cosmic ray albedo neutron decay and trapped solar energetic protons (Dragt et al., 1966; Farley et al., 1970; Freden & White, 1962; Selesnick et al., 2007; Selesnick et al., 2010; Selesnick et al., 2014; Singer, 1958). Cosmic ray albedo neutron decay is the dominant source for the radiation belt protons with high energies (e.g., $\geq$100 MeV) or at low L (e.g., $L{\leq}1.3$), while radiation belt protons with lower energies and at higher L are dominated by the solar energetic protons (Jentsch, 1981; Selesnick et al., 2007). The energy loss and the loss of radiation belt protons are related to the neutral atmosphere, the ionosphere, and plasmasphere through the ionization, and nuclear reactions or interactions with free electrons (Selesnick et al., 2007). In addition, the radial diffusion, pitch angle diffusion, and adiabatic compression or expansion during the varying geomagnetic field can also influence the distribution of radiation belt protons (Albert et al., 1998; Croley et al., 1976; Selesnick et al., 2007; Shao et al., 2009). Therefore, the proton radiation belt is not absolutely stable, exhibiting changes on various time scales, such as the solar cycle variation, the drift of South Atlantic Anomaly (SAA), and the appearance of a second proton radiation belt (e.g., Badhwar, 1997; Blake et al., 1992; Qin et al., 2014; Selesnick et al., 2007).

Radiation belt protons threaten the safe operation of satellites flying in low Earth orbit (LEO) and medium Earth orbit altitudes (e.g., LEO satellites and HEO satellites), potentially damaging these satellites through total ionizing dose, displacement, and single-event effects. They also pose risk to space station astronauts when crossing the SAA (e.g., Berger, 2008; Duzellier, 2005; Miroshnichenko, 2003; Samwel et al., 2008). Therefore, it is of both scientific and practical significance to quantify the spatial distribution of the proton radiation belt, to comprehend its dynamic variations, and to develop reliable models for prediction.

The NOAA POES (National Oceanic and Atmospheric Administration, Polar Operational Environmental Satellites) and EUMETSAT MetOp (European Organisation for the Exploitation of Meteorological Satellites, Meteorological Operational) satellites have been continuously monitoring the energetic protons in the low-altitude proton radiation belt since 1978. This long-term archive consists of energetic electron and proton measurements in unidirectional differential fluxes and omnidirectional integral fluxes (i.e., Evans & Greer, 2006; Green, 2013a, 2013b, 2013c; Machol, 2012; Ni et al., 2014; Redmon et al., 2017). These data, covering the period of about 3.5 solar cycles, are valuable for investigating the proton radiation belt. However, due to the degradation of energetic proton detectors onboard the satellites (Galand & Evans, 2000), the inconsistency of calibration among these satellites' measurements (Qin et al., 2014), and data bifurcations shown in Figure 3-3 of Huston and Pfitzer (1998) or discussed in section 2.2, these measurements need to be processed and recalibrated carefully to a common reference, yielding a long-term database for quantitative studies.

For the energetic proton unidirectional differential fluxes, the major issue is that these detectors degrade with time due to radiation damage (Galand & Evans, 2000). To deal with this, Asikainen and Mursula (2011) and Asikainen et al. (2012) derived one set of potential correction factors for the three lowest energetic proton channels, Ødegaard (2013) reported potential correction factors for the two lowest energetic proton channels, and Sandanger et al. (2015) estimated correction factors for all five energetic proton channels. Based on those previous studies, the correction factors depend on the energy channel, the orientation of the detectors, and the observation time. In addition, Yando et al. (2011) confirmed that the directional proton telescope of NOAA POES MEPED instrument is polluted by the relativistic electrons through the Monte Carlo simulations. Therefore, the relativistic electron contamination should be considered for the correction factors of energetic proton channels.

For the energetic proton omnidirectional integral fluxes, there are two major issues. One is the data bifurcation, and the other is the calibration inconsistency among the POES and MetOp satellites' measurements. Huston and Pfitzer (1998) first presented the data bifurcation, called it bifurcation structure, and provided an explanation. They thought that the bifurcation was due to an ephemeris timing error and could be eliminated by the time shift of satellite ephemeris that can be determined by minimizing the scatter of the cross-comparison. The calibration inconsistency among the NOAA POES satellites' measurements has rarely been reported. Qin et al. (2014) pointed out that data from different NOAA POES satellites can be cross calibrated in order to obtain a consecutive evolution of the SAA, while they did not introduce how to recalibrate the data. The traditional approach is to multiply the fluxes by a constant correction factor or a set of correction factors varying with time or locations, similar to the recalibration by Sandanger et al. (2015).

Through investigating the data of energetic proton omnidirectional integral fluxes from the NOAA POES and EUMETSAT MetOp satellites in the present study, it is found that there are at least two categories of data bifurcations. More explanations are required for these bifurcations, and the traditional approach of correction factors is too rough to recalibrate the data. In this paper, we will illustrate all categories of the data bifurcations, investigate their underlying explanations, show the calibration inconsistency among the POES and MetOp satellites' measurements, and present a new method to recalibrate the data.

Following this section, the paper is organized as follows. A description of the NOAA POES and EUMETSAT MetOp SEM instruments and data processing is given in section 2.1. Section 2.2 presents the issues associated with the energetic proton omnidirectional integral fluxes, including the calibration inconsistency, the data bifurcations, and the erroneous data. Section 3 provides our cross calibration technique for >16 MeV proton omnidirectional integral fluxes. Section 4 compares recalibrated observations and predictions from the AP8 model. Section 5 discusses our results, and section 6 summarizes the conclusions.

2. Data

2.1. Instrumentation and Data Processing

The Space Environment Monitor (SEM-1 and SEM-2) onboard the NOAA POES and EUMETSAT MetOp (SEM-2 only) satellites has been continuously measuring the charged particle environment of LEO Sun-synchronous orbits since 1978, providing a rich data set for studying long-term behaviors. These orbits all have an inclination of ~98°, an altitude of 800-900 km, and a period of ~100 min. With respect to the data used herein, satellites from TIROS-N, NOAA-06, NOAA-07, NOAA-08, NOAA-10, NOAA-12, and NOAA-14 carried the first version of SEM (SEM-1), and NOAA-15, NOAA-16, NOAA-17, NOAA-18, NOAA-19, and MetOp-02 (MetOp-A) were equipped with the new version of SEM (SEM-2). The MEPED instrument (Medium Energy Proton and Electron Detector) is a portion of the SEM. It consists of two sensor assemblies: the directional electron and proton detectors and the omnidirectional proton detectors. Here we only use the data of energetic proton omnidirectional integral fluxes from POES and MetOp satellites. The MEPED effective energy ranges are slightly different from SEM-1 to SEM-2 (i.e., Evans & Greer, 2006; Green, 2013a, 2013b, 2013c; Machol, 2012). SEM-1 was equipped with three omnidirectional proton detectors with a full-opening view angle of 120° for energies >16, >36, and >80 MeV, while SEM-2 has four omnidirectional proton detectors with a full-opening view angle of 120° for energies >16 and >35 MeV, and 180° for energies >70 and >140 MeV. The central axis of each omnidirectional detector is parallel to the viewing axis of the 0° MEPED proton and electron detector telescope units (Evans & Greer, 2006). Although NOAA-15 to NOAA-19 and MetOp-02 are equipped with SEM-2, there are slight variations in the exact pointing of the MEPED suite. The central axis of the MEPED package on POES satellites is rotated twice: 9° off the −X direction, and an additional 9.08° off the +Y direction, where the X axis points earthward and the Y axis points opposite to the velocity direction of the satellite (Green, 2013a). However, the MEPED package on the MetOp-02 satellite has no rotations (Green, 2013a). More details about SEM-1 and SEM-2 are given by Raben et al. (1995), Evans and Greer (2006), Machol (2012), and Green (2013b).

Archived data from NOAA POES and MetOp satellites in the binary format with full time resolution are available from https://satdat.ngdc.noaa.gov/sem/poes/data/raw/swpc/. Each 8-second logical record of the archived data contains the time, orbital parameters, magnetic field parameters, the counts of four 2-s accumulation for each proton channel, and so on. Due to the existing 8-s orbital parameters, we sum the counts of four 2-s accumulation to get the 8-s averaged count rates for each proton channel. We also convert the averaged count rates to omnidirectional integral fluxes, and recalculate geomagnetic field parameters.

For SEM-1, the archived records of three proton detectors (P6, P7, and P8) provide the 16 to 215 MeV, 36 to 215 MeV, 80 to 215 MeV proton counts, respectively. Their 8-s averaged count rates are obtained and labeled as CR_6, CR_7, and CR_8, respectively. P6 (P7) detector not only records 16-80 MeV (36-80 MeV) protons with geometric factor 1.178 $cm^2 \cdot sr$, but also records 80 to 215 MeV protons with geometric factor 2.701 $cm^2 \cdot sr$, and P8 only has one geometric factor 2.701 $cm^2 \cdot sr$, as listed in Table 2.2 of Raben et al. (1995). Therefore, the omnidirectional integral fluxes (J_6, J_7, and J_8) in $cm^{-2} \cdot s^{-1}$ for energies >16, >36, and >80 MeV are given by

$$\begin{cases} J_6 = (CR_6 - CR_8)/1.178 \cdot 4\pi + J_8 \\ J_7 = (CR_7 - CR_8)/1.178 \cdot 4\pi + J_8 \\ J_8 = CR_8/2.701 \cdot 4\pi \end{cases} \tag{1}$$

For SEM-2, the archived records of four proton detectors (P6, P7, P8, and P9) provide the 16 to 35 MeV, 35 to 70 MeV, 70 to 140 MeV, and 140 to 500 MeV proton counts, respectively. The averaged directional integral fluxes in $cm^{-2} \cdot s^{-1} \cdot sr^{-1}$ for energies >16, >35, >70, and >140 MeV, which are multiplied by $4 \cdot \pi$ to estimate the omnidirectional integral fluxes (J_6, J_7, J_8, and J_9), are given as Case 1 in Appendix F from Evans and Greer (2006). The omnidirectional integral fluxes above neglect the contribution of protons with energies larger than the maximum detectable proton energy (215 MeV for SEM-1 and 500 MeV for SEM-2), because the differential flux of energetic protons in radiation belt decays substantially following an exponential decay law.

In this 8-s archive, several geomagnetic field parameters are included: magnetic L value (McIlwain, 1961), local magnetic field vector, the location and the magnetic field vector at the foot of magnetic field line, etc (Evans & Greer, 2006; Raben et al., 1995). These parameters are related to the selected geomagnetic field
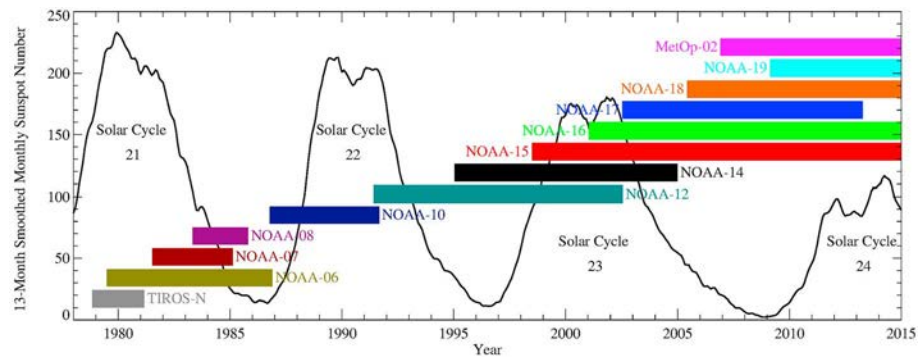
Figure 1. The operation periods of POES and MetOp satellites before 2015. The color bars show the operation period of each satellite. The black curve is the 13-month smoothed monthly sunspot number for the definition of solar cycles.

model. In the archived record, the magnetic field and the L value are determined by a simple table lookup, which is not accurate enough (Huston & Pfitzer, 1998). In this study, for improvements we use the International Geomagnetic Reference Field (IGRF) internal field model (Thébault et al., 2015) and Olson & Pfitzer, 1977 external field model (OPQ77) to calculate the McIlwain's L value (L_m; McIlwain, 1961), local magnetic field strength (B), and the minimal magnetic field strength along the magnetic field line (B_0). In addition, we also calculate the magnetic local time (MLT) and location in SM coordinates. The coefficients of the IGRF model are updated every 5 years and hosted by NOAA's NCEI, and the IGRF model coefficients for any specified day can be obtained through linear interpolation. The routines to compute the parameters above are provided by the International Radiation Belt Environment Modeling library (IRBEM-LIB) available from https://craterre.onecert.fr/prbem/irbem/description.html. In the OPQ77 routine, when the radial distance is less than 2 R_E ($1R_E$=6371.2 km), the magnetic field from the OPQ77 model is set to be zero; that is, the geomagnetic field is estimated only by the IGRF model. Therefore, the OPQ77 model is only used when L_m is larger than about 2 for the current study.

In this paper, only >16 MeV proton omnidirectional integral fluxes (abbreviated as >16 MeV proton fluxes hereafter) are used to do the cross calibration and to study the spatio-temporal variations of the proton radiation belt, because it is the common energy channel between SEM-1 and SEM-2. The data with an 8-s resolution cover the period from 1978 to 2014, about 3.5 solar cycles. The operation periods of POES and MetOp satellites before 2015 are shown in Figure 1. Each satellite has an overlapping operation period with at least one other satellite to form an overall continuous operation period from 1978 to 2014 during Solar Cycles 21-24.

2.2. Data Issues

The processing described above yields important updates to the energetic proton flux data set. However, these data are still unreadily usable for long-term quantitative analysis of the proton radiation belt in the SAA directly, because there are at least three remaining critical issues: calibration inconsistency, data bifurcations, and erroneous data.

Figure 2 shows the distribution of >16 MeV proton fluxes with $|B/B_0-1.0|\leq0.003$ for five L_m bins from POES and MetOp satellites from 1978 to 2014. All data in Figure 2a are at or near the geomagnetic equator ($B/B_0=1$), the five bins are those of $|L_m-1.12|\leq0.002$, $|L_m-1.14|\leq0.002$, $|L_m-1.16|\leq0.002$, $|L_m-1.18|\leq0.002$, and $|L_m-1.20|\leq0.002$, and they are plotted from bottom to top in Figure 2a, respectively. Their altitudes and MLTs are shown in Figures 2b and 2c. The data from different satellites, which are listed in the top of Figure 2, are illustrated with different colors. It is shown that the >16 MeV proton fluxes for the overlapping time, L_m, and B/B_0 from different satellites are inconsistent. The differences between pairs are clear: NOAA-06 and NOAA-07, NOAA-06 and NOAA-08, NOAA-14 and NOAA-15, NOAA-14 and NOAA-16, NOAA-14 and NOAA-17. Furthermore, >16 MeV proton fluxes from SEM-1 are larger than those from SEM-2. Normally, SEM-2 should observe more >16 MeV protons, because its maximum detectable proton energy (500 MeV) is larger than that of SEM-1 (215 MeV). Combined with Figure 2c, it is found that the inconsistent results still
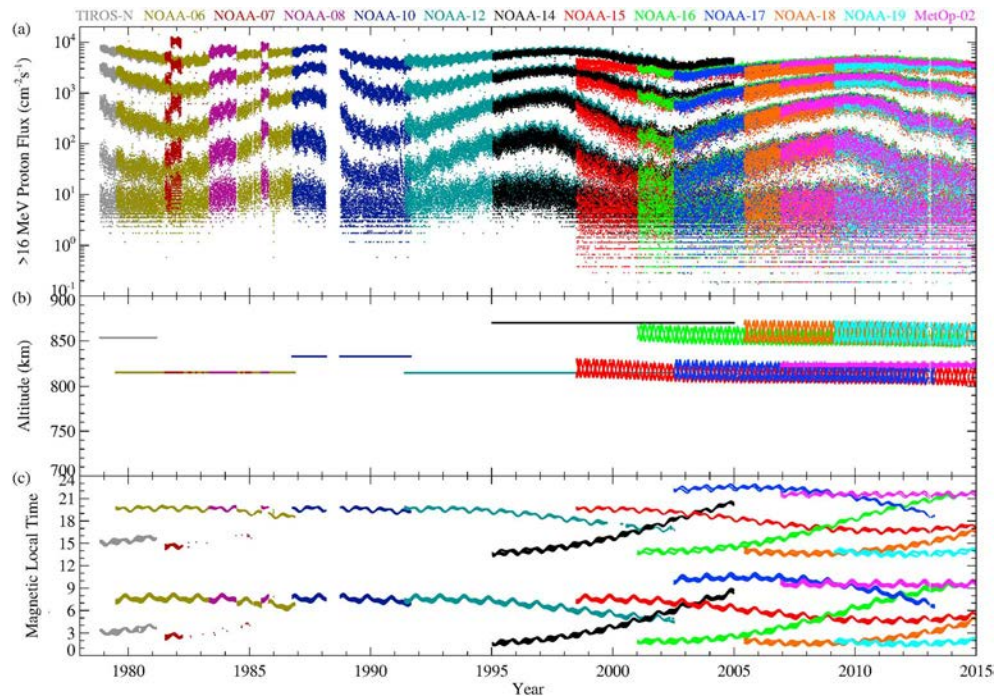
Figure 2. The distribution of >16 MeV proton fluxes with $|B/B_0-1.0|\leq0.003$ for five L_m bins from POES and MetOp satellites from 1978 to 2014. In the panel (a), five bins plotted from bottom to top are the bins of $|L_m-1.12|\leq0.002$, $|L_m-1.14|\leq0.002$, $|L_m-1.16|\leq0.002$, $|L_m-1.18|\leq0.002$, and $|L_m-1.20|\leq0.002$. Panels (b) and (c) display the altitudes and magnetic local times corresponding to the >16 MeV proton fluxes plotted in the panel (a). The data from different satellites, listed above the panel (a), are plotted with different colors.

exist at the same MLT. This inconsistency is mainly due to the calibration inconsistency among the POES and MetOp satellites' measurements and possibly satellite ephemeris/orbit uncertainty. As shown in Figure 2b, the archived data of TIROS-N, NOAA-06, NOAA-07, NOAA-08, NOAA-10, NOAA-12, and NOAA-14 using the SEM-1 detector only provide a smoothed, constant orbital altitude. The deviation of orbital data can also cause the inconsistency of observations. This inconsistency can be significantly reduced or even eliminated through the cross calibration, which will be described in detail in section 3.

The calibration inconsistency above appears in the data from different satellites. However, there also exist the different observations from each POES or MetOp satellite for overlapping time, L_m, and B/B_0. We take the data of >16 MeV proton fluxes from NOAA-15 as an example. Figure 3 shows the distribution of >16 MeV proton fluxes with $|B/B_0-1.0|\leq0.001$ (a and d), $|L_m-1.26|\leq0.001$ (b and e), and with $|L_m-1.80|\leq0.001$ (c and f) from NOAA-15 in 2008. In Figures 3a–3c, the red and green dots are the data with MLT≤12:00 and MLT>12:00, respectively. In Figures 3d–3f, the color of dots represents the magnetic latitude (MLAT) value corresponding to their bottom color bars. As shown in Figures 3a, 3e, and 3f, there are obvious upper and lower branches, which are referred as a bifurcation by Huston & Pfitzer, 1998. For the data at or near the geomagnetic equator, upper and lower branches can be distinguished by MLT as displayed in Figure 3a; however, it does not work for the bins with $|L_m-1.26|\leq0.001$ in Figure 3b and $|L_m-1.80|\leq0.001$ in Figure 3c. Fortunately, their upper and lower branches can be distinguished by the MLAT as illustrated in Figures 3e and 3f, but it is not suitable for the data with $|B/B_0-1.0|\leq0.001$ as shown in Figure 3d. This means that the data bifurcations in different regions need different methods to distinguish the upper and lower branches. For the cross calibration in section 3, only data with MLT≤12:00 are used. For the bifurcations in these data, only upper branches are adopted to get available data as many as possible, that is, Figure 3e. The reasons for the data bifurcations will be discussed in section 5.

The measurements of the radiation belts often contain erroneous data, due to various reasons including contamination, saturation, background noise, and invalid measurement (Bourdarie et al., 2008). The measurements of POES and MetOp satellites also have the same issue. Figure 4 shows the distribution of >16 MeV
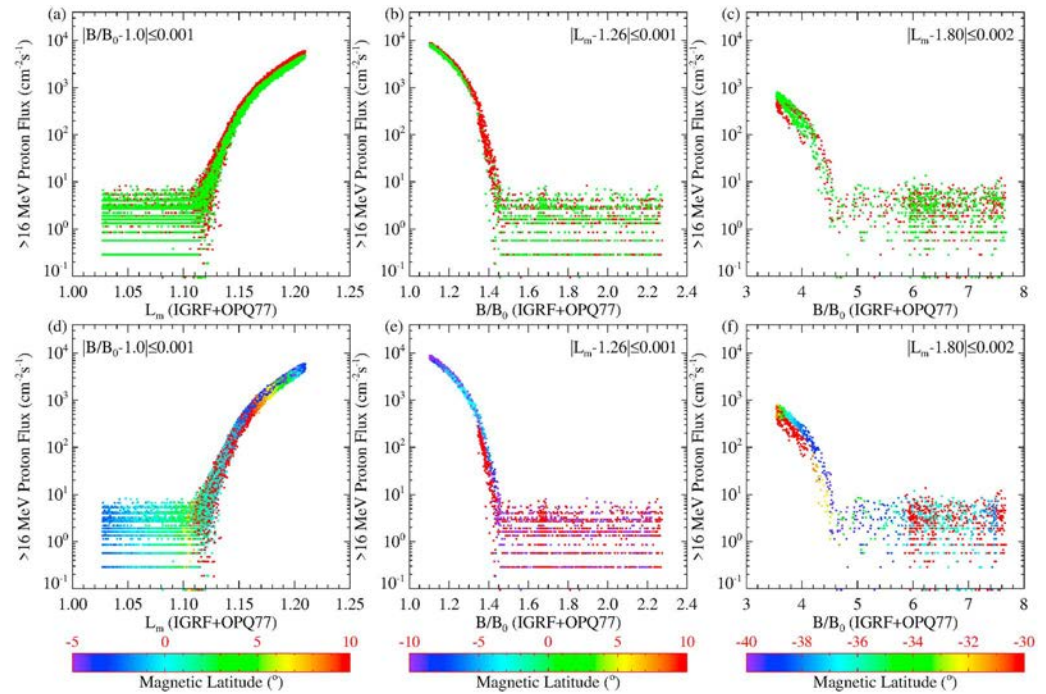
Figure 3. The distribution of >16 MeV proton fluxes for three bins from NOAA-15 in 2008. Three bins are the data with $|B/B_0-1.0|\leq0.001$ in panels (a) and (d), with $|L_m-1.26|\leq0.001$ in panels (b) and (e), and with $|L_m -1.80|\leq0.001$ in panels (c) and (f). In panels (a), (b), and (c), the red dots are the data with MLT≤12:00, and the green dots are the data with MLT from 12:00 to 24:00. In panels (d), (e), and (f), the color of dots represents the magnetic latitude value corresponding to their bottom color bars, respectively.

proton fluxes with $|B/B_0-1.0|\leq0.003$ and MLT≤12:00 from POES and MetOp satellites, listed in the top of the figure with different colors, during the period from 1978 to 2014. The scattered points and the points with constant fluxes (horizontal lines) in Figure 4a are clearly erroneous. In order to remove these erroneous data, we select them from every 2-month segment of each POES or MetOp satellite by manual processing. Figure 4b presents the distribution of data after removing the erroneous data. It shows that almost all erroneous data are filtered out. In the high-latitude regions, some scattered data may be from the solar proton events. These points are also removed, because we focus on the cross calibration to study the long-
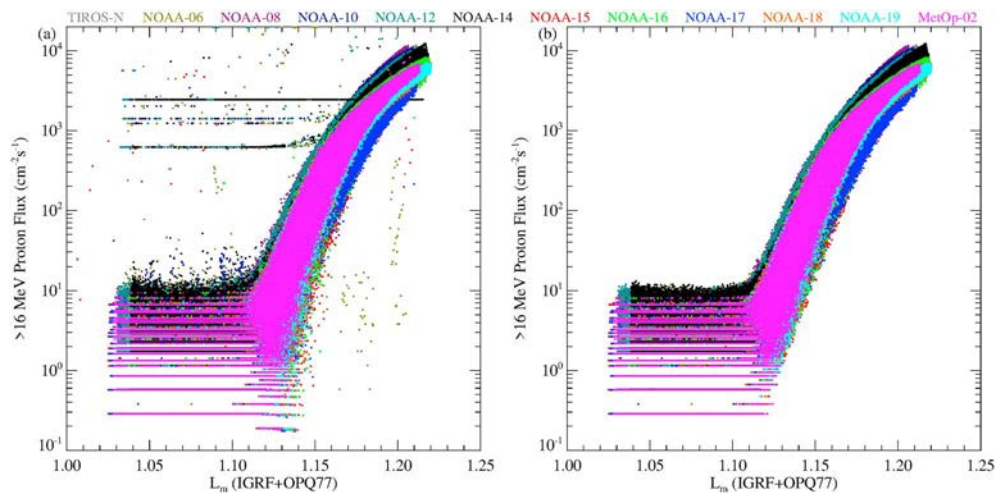

Figure 4. The distribution of >16 MeV proton fluxes with $|B/B_0-1.0|\leq0.003$ and MLT≤12:00 from POES and MetOp satellites during the period from 1978 to 2014: (a) the original data; (b) the data after removing the erroneous data. The data from different satellites, listed in the top of figure, are plotted with different colors.

term variations of the proton radiation belt in the SAA. If the data of protons from solar proton events are not scattered, they will be left to maintain the continuity of data.

In addition, the data from NOAA-07 are abandoned due to a number of reasons including that there are abrupt changes in the data, the period of its available data is only several months, and NOAA-06 has available data during this period as shown in Figure 2a.

Finally, only >16 MeV proton fluxes with MLT≤12:00 from POES and MetOp satellites, excluding NOAA-07, are used for the investigation. After data processing, these data points do not include the erroneous data and the lower branches of bifurcations.

3. Cross Calibration

As shown in Figure 2a, >16 MeV proton fluxes for the overlapping time, L_m, and B/B_0 from different satellites are more or less different, so the cross calibration among POES and MetOp satellites' measurements need to be done before quantitative analysis.

The principle of cross calibration is that the measurements of the same parameter (>16 MeV proton flux) by different satellites for the same time, L_m, and B/B_0 are consistent. Because >16 MeV proton fluxes vary very slowly and each satellite has an overlapping operation period with at least one other satellite as shown in Figure 2a, it ensures sufficient enough data for cross calibration.

To know how the inconsistency of measurements at the same L_m and B/B_0 between each both NOAA satellites changes with L_m and B/B_0, we take the data of >16 MeV proton fluxes from NOAA-14 and NOAA-15 in 1999 as an example.

Figure 5 shows the inconsistency and the cross calibration of >16 MeV proton fluxes with different L_m bins between NOAA-14 and NOAA-15 in 1999. Figure 5a plots all original data with MLT≤12:00 from NOAA-14 in black and from NOAA-15 in green, and their L_m-bin data are in red and in blue, respectively. The seven L_m bins in Figure 5a from left to right are $|L_m$-1.15$|\leq$0.004, $|L_m$-1.20$|\leq$0.005, $|L_m$-1.30$|\leq$0.01, $|L_m$-1.45$|\leq$0.015, $|L_m$-1.60$|\leq$0.02, $|L_m$-1.80$|\leq$0.02, and $|L_m$-2.00$|\leq$0.02, respectively. After removing the lower branches of bifurcations and the erroneous data mentioned in section 2.2, the data of L_m bins for recalibration are displayed in Figure 5b. It clearly indicates the measurement inconsistency from NOAA-14 (red) and NOAA-15 (blue). Note that >16 MeV proton fluxes from NOAA-14 are obviously larger than those from NOAA-15. To determine a statistically sound relationship, the data in each L_m bin are divided into different B/B_0 bins, and their averaged fluxes are obtained and plotted in Figure 5b as black and cyan dots. Figures 5d–5f illustrate the relationship of these averaged data from NOAA-14 and NOAA-15 with different L_m bins in different colors. Figure 5d shows the ratios of >16 MeV proton fluxes from NOAA-14 to those from NOAA-15, and Figure 5e displays the ratios of the base 10 logarithm of >16 MeV proton fluxes from NOAA-14 to those from NOAA-15. It indicates that these ratios are not constant, but change with L_m and B/B_0. When these averaged data are plotted in the log-log coordinates as shown in Figure 5f, it is found that the relationship of NOAA-14 and NOAA-15 inconsistent measurements with different L_m in the log-log coordinates is consistent in the interval of overlapping data, and it is almost independent of L_m. Therefore, the distribution of dots in Figure 5f can be described well by a third-degree polynomial function:

$$y = a_0 + a_1 \cdot x + a_2 \cdot x^2 + a_3 \cdot x^3 \tag{2}$$

where x and y are the base 10 logarithm of >16 MeV proton fluxes from NOAA-14 and NOAA-15 at the same L_m and B/B_0, respectively. The values of fitted coefficients, the correlation coefficient of x and y (COR1), and the correlation coefficient of y_{fit} and y (COR2) are listed in Table 1, where y_{fit} is the base 10 logarithm of recalibrated fluxes. The black curve in Figure 5f is the fitted result. Based on this fitted curve, the data from NOAA-14 can be recalibrated to the NOAA-15 measurements. Figure 5c demonstrates that the recalibrated data from NOAA-14 are well consistent with the data from NOAA-15. In order to further demonstrate how well the data are matched, we have added the upper and lower red curves in Figure 5f. They correspond to $Flux_{upper} = 10^{y_{fit}(x)} \cdot (1.0 + 0.45)$ and $Flux_{lower} = 10^{y_{fit}(x)} \cdot (1.0 - 0.35)$, respectively, where $10^{y_{fit}(x)}$ is the fitted flux. If we take the slop of fitted curve as 1, the span between the upper (lower) red curve and the fitted curve is about $31.8\% \cdot 10^{y_{fit}(x)}$ ($24.7\% \cdot 10^{y_{fit}(x)}$). In Figure 5f, only three points are above the upper red curve and only two points are under the lower red curve.
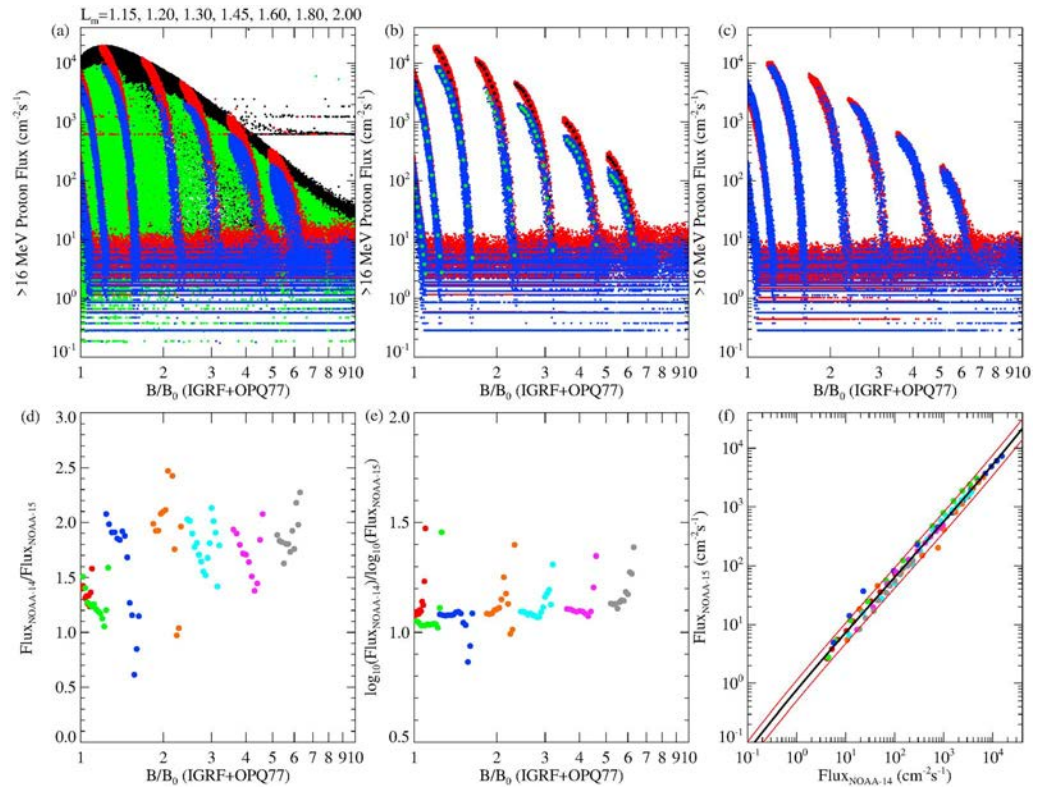
Figure 5. The inconsistency and the cross calibration of >16 MeV proton fluxes with different L_m bins from NOAA-14 and NOAA-15 in 1999. Their L_m bins in panel (a) from left to right are $|L_m$-1.15$|\leq$0.004, $|L_m$-1.20$|\leq$0.005, $|L_m$-1.30$|\leq$0.01, $|L_m$-1.45$|\leq$0.015, $|L_m$-1.60$|\leq$0.02, $|L_m$-1.80$|\leq$0.02, and $|L_m$-2.00$|\leq$0.02, respectively. Panels (a), (b), and (c) plot the original data, the data for the recalibration and the recalibrated data, respectively. The MLT of these data are from 00:00 to 12:00. In panel (a), black dots (all data) and red dots (the data with different L_m bins) are from NOAA-14, and green dot (all data) and blue dots (the data with different L_m bins) are from NOAA-15. In panels (b) and (c), the data of L_m bins have removed the lower branches of bifurcations and the erroneous data. In panels (b), the red dots and blue dots are the data for the recalibration from NOAA-14 and NOAA-15, respectively, and the black dots and the cyan dots are the averaged values of each B/B_0 bin for the different L_m bins. Panels (d), (e), and (f) show the relationships between NOAA-14 and NOAA-15 measurements with different L_m bins in different colors. The black curve in panel (f) is the fitted result for the relationship between NOAA-14 and NOAA-15 measurements, and the red curves demonstrate how well the data are fitted. In panel (c), the data from NOAA-14 have been recalibrated to the NOAA-15 measurements by the fitted curve.

Figure 6 shows the inconsistent and cross calibrated >16 MeV proton fluxes with different B/B_0 bins from NOAA-14 and NOAA-15 in 1999. The B/B_0 bins plotted in Figure 6a from left to right are $|B/B_0$-1.0$|\leq$ 0.003, $|B/B_0$-1.2$|\leq$0.015, $|B/B_0$-1.5$|\leq$0.03, $|B/B_0$-1.9$|\leq$0.04, $|B/B_0$-2.4$|\leq$0.08, and $|B/B_0$-4.0$|\leq$0.12, respectively. The data of these bins in Figures 6b and 6c do not include the lower branches of the bifurcations or erroneous data mentioned in section 2.2. Figure 6 also shows that the ratios of >16 MeV proton fluxes from NOAA-14 to those from NOAA-15, or the ratios of the base 10 logarithm of >16 MeV proton fluxes from NOAA-14 to those from NOAA-15 change with L_m and B/B_0. However, the relationship of NOAA-14 and

Table 1
The Values of Fitted Coefficients for the Cross Calibration of >16 MeV Proton Fluxes Between NOAA-14 and NOAA-15 Satellites in Figures 5f, 6f, and 7c

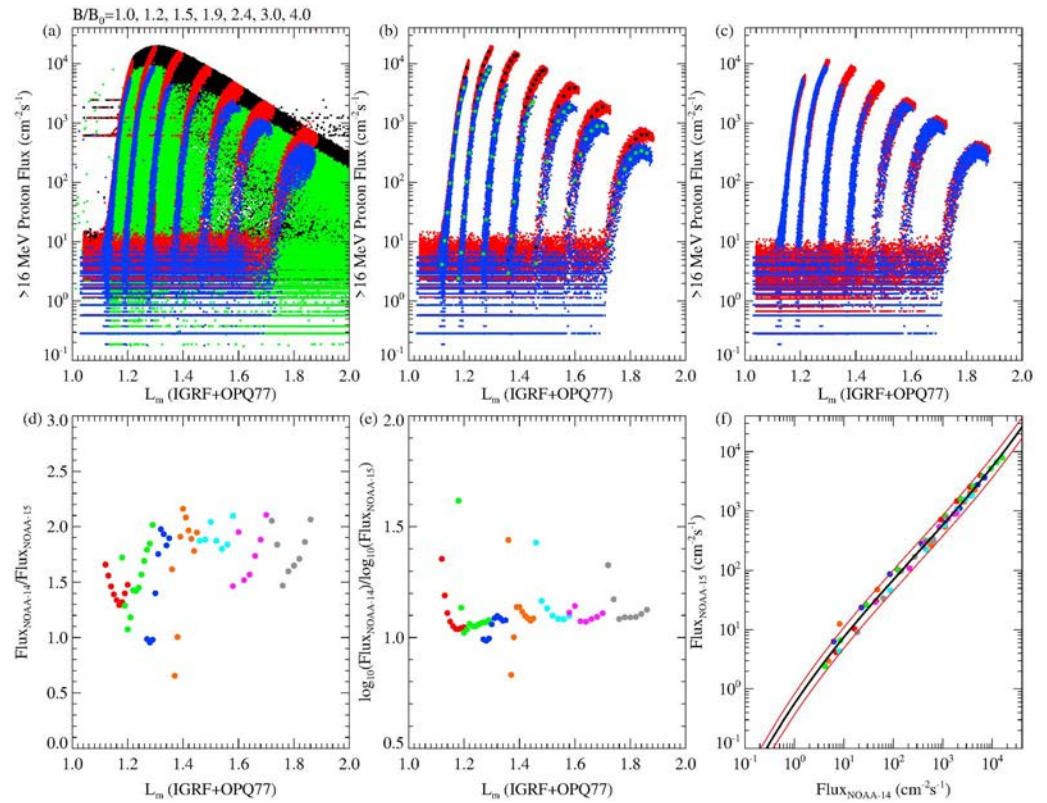| Figures	Data for fitting	Fitted results					
		a_0	a_1	a_2	a_3	COR1	COR2
Figure 5f	Different L_m bins in 1999	-0.113	1.003	-0.0313	0.00507	0.993696	0.993716
Figure 6f	Different B/B_0 bins in 1999	-0.249	1.239	-0.133	0.0183	0.995287	0.995425
Figure 7c	$|B/B_0$-1.0$|\leq$0.003 bins in different years	-0.429	1.308	-0.897	0.00701	0.998783	0.999431

Figure 6. The inconsistency and the cross calibration of >16 MeV proton fluxes with different B/B_0 bins from NOAA-14 and NOAA-15 in 1999. The B/B_0 bins in panel (a) from left to right are $|B/B_0$-1.0$|\leq$0.003, $|B/B_0$-1.2$|\leq$0.015, $|B/B_0$-1.5$|\leq$0.03, $|B/B_0$-1.9$|\leq$0.04, $|B/B_0$-2.4$|\leq$0.08, and $|B/B_0$-4.0$|\leq$0.12. It has the same format as Figure 5.

NOAA-15 inconsistent measurements with different B/B_0 in the log-log coordinates is consistent in the interval of overlapping data, and they are almost independent of B/B_0. Equation (2) can describe their relationship well. The values of fitted coefficients, COR1 and COR2 are listed in Table 1. By the black fitted curve in Figure 6f, the data from NOAA-14 are recalibrated, and they are now consistent with the data from NOAA-15 as shown in Figure 6c. In Figure 6f, we also plot the red curves of $Flux_{upper} = 10^{y_{fit}(x)} \cdot (1.0 + 0.45)$ and $Flux_{lower} = 10^{y_{fit}(x)} \cdot (1.0 - 0.35)$, and only 1 point is above the upper red curve or under the lower red curve.

The results above prove that the calibration inconsistency of measurements at the same L_m and B/B_0 between NOAA-14 and NOAA-15 can be mitigated obviously using a third-degree polynomial function and that the relationship of their inconsistent measurements in the log-log coordinates is almost independent of L_m and B/B_0. Next, we intend to prove that the fitted curves from Figures 5 and 6 are almost identical in the valid flux range of the fitted data, and the relationship of their inconsistent measurements between NOAA-14 and NOAA-15 is almost independent of time.

Because the relationship of the inconsistent measurements is almost independent of L_m and B/B_0, we can use the data near the geomagnetic equator to examine whether this relationship changes with time. Figures 7d-7i show the inconsistent and cross calibrated >16 MeV proton fluxes for $|B/B_0$-1.0$|\leq$0.003 from NOAA-14 and NOAA-15 in 1999, 2000, 2001, 2002, 2003, and 2004. Figures 7a and 7b display the ratios of >16 MeV proton fluxes from NOAA-14 to those from NOAA-15, and the ratios of the base 10 logarithm of >16 MeV proton fluxes from NOAA-14 to those from NOAA-15 change with L_m and time. However, the relationship of NOAA-14 and NOAA-15 inconsistent measurements with different time in the log-log coordinates is consistent in the interval of overlapping data, and it is almost independent of time as shown in Figure 7c. We also use equation (2) to fit their relationship, and the fitted result is shown as the black curve in Figure 7c. The values of fitted coefficients, COR1 and COR2 are listed in Table 1. Figures 7j-7o demonstrate that the recalibrated data from NOAA-14 are consistent with the data from NOAA-15.
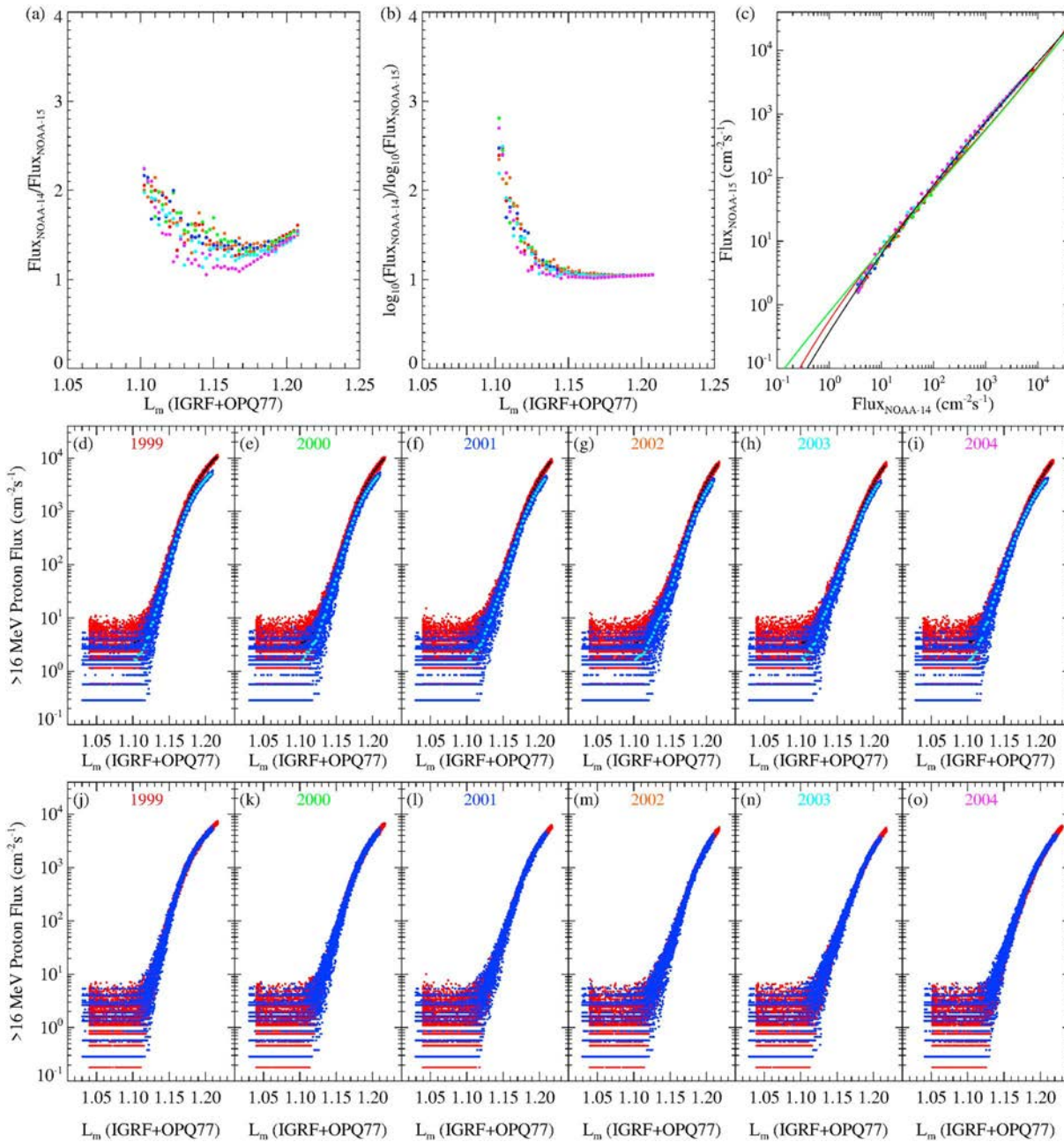
Figure 7. The inconsistency and the cross calibration of >16 MeV proton fluxes with $|B/B_0 - 1.0| \leq 0.003$ from NOAA-14 and NOAA-15 in 1999, 2000, 2001, 2002, 2003, and 2004. The formats of panels are same as Figure 5. Panels (a), (b), and (c) show the relationships of measurements between NOAA-14 and NOAA-15 in 1999, 2000, 2001, 2002, 2003, and 2004 in the red, green, blue, orange, cyan, and magenta colors, respectively. In panel (c), the black curve is the fitted result, and the green and red curves are the fitted results from Figures 5c and 6c, respectively. Panels (d)-(i) show the data before recalibration, and panels (j)-(o) show the data after recalibration.

In Figure 7c, the green curve and the red curve are from Figures 5c and 6c, respectively. When the fluxes from NOAA-14 are larger than $3\,\mathrm{cm^{-2} \cdot s^{-1}}$ and less than $10{,}000\,\mathrm{cm^{-2} \cdot s^{-1}}$, both curves almost coincide with each other, and the black curve is also similar to both curves. Only when the fluxes from NOAA-14 are between 200 and $10{,}000\,\mathrm{cm^{-2} \cdot s^{-1}}$, the black curve is slightly above both curves. From Figures 5c and 6c, it is found that when the fluxes are between 200 and $10{,}000\,\mathrm{cm^{-2} \cdot s^{-1}}$, the recalibrated fluxes from NOAA-14 are somehow less than the fluxes from NOAA-15 in the region close to the geomagnetic equator. However, they coincide with each other in the region away from the geomagnetic equator. That is, it is

Table 2
The Cross Calibration Information of >16 MeV Proton Fluxes Among POES and MetOp Satellites and the Values of Fitted Coefficients

Satellites for cross calibration	Period of data for fitting (year/month/day)	Data for fitting (B/B_0 Bin)	a_0	a_1	a_2	a_3	COR1	COR2
TIROSN--NOAA-06	1979/07/01--1979/11/01	1.00 ± 0.003 1.15 ± 0.02	0.0320	0.989	0.00349	-0.000181	0.999873	0.999875
NOAA-08--NOAA-06	1985/05/01--1986/01/01	1.00 ± 0.003 1.15 ± 0.02	0.179	0.502	0.205	-0.0250	0.999111	0.999744
NOAA-06--NOAA-10	1986/10/01--1986/12/01	1.00 ± 0.003 1.15 ± 0.02	0.125	0.586	0.175	-0.0204	0.999242	0.999829
NOAA-10--NOAA-12	1991/05/01--1991/10/01	1.00 ± 0.003 1.15 ± 0.02	-0.137	1.525	-0.221	0.0257	0.998093	0.999514
NOAA-12--NOAA-15	1998/07/01--1998/11/01	1.00 ± 0.003 1.15 ± 0.02	-0.172	0.723	0.158	-0.0237	0.999637	0.999819
NOAA-14--NOAA-15	1998/07/01--1998/11/01	1.00 ± 0.003 1.15 ± 0.02	-0.552	1.467	-0.145	0.0117	0.998064	0.999561
NOAA-16--NOAA-15	2009/06/01--2009/08/01	1.00 ± 0.003 1.05 ± 0.015	0.000479	0.971	0.0131	-0.00158	0.999675	0.999680
NOAA-17--NOAA-15	2009/06/01--2009/08/01	1.00 ± 0.003 1.15 ± 0.02	0.0217	0.945	0.0377	-0.00593	0.999595	0.999607
NOAA-18--NOAA-15	2009/06/01--2009/08/01	1.00 ± 0.003 1.15 ± 0.02	-0.0123	1.131	-0.0615	0.00883	0.999663	0.999711
NOAA-19--NOAA-15	2009/06/01--2009/08/01	1.00 ± 0.003 1.15 ± 0.02	-0.00957	1.184	-0.103	0.0163	0.999692	0.999781
MetOp-02--NOAA-15	2009/06/01--2009/08/01	1.00 ± 0.003 1.15 ± 0.02	-0.0720	1.181	-0.0720	0.00792	0.999495	0.999730

impossible to recalibrate all data from NOAA-14 very well by one fitted curve. It may be due to the deviation of the geomagnetic field model for calculating L_m, B and B_0, or other reasons. Because there is only small difference among three curves in Figure 7c, this difference can be ignored.

Based on the analysis above, the relationship between NOAA-14 and NOAA-15 measurements is independent of L_m, B/B_0, and time, so the fitted curves for recalibration of >16 MeV proton fluxes among POES and MetOp satellites can be obtained from the overlapping data close to the geomagnetic equator at any period of time. This characteristic exists in the data from any two satellites among POES and MetOp satellites. Based on equation (2) and the data listed in the second and third columns of Table 2, the values of fitted coefficients for the recalibration of >16 MeV proton fluxes from POES and MetOp satellites are obtained as listed from the forth to seventh columns of Table 2. In the first column of Table 2, the data from the left-side satellite are recalibrated to the measurements from the right-side satellite. The eighth and ninth columns list the COR1 and COR2. It presents that the correlation coefficients increase a little after calibration for all satellites. Figure 8 shows the fitted curves for the recalibration of >16 MeV proton fluxes among POES and MetOp satellites. The green dots are the averaged data with $|B/B_0\text{-}1.0|\leq0.003$, and the red dots are the averaged data with $|B/B_0\text{-}1.15|\leq0.02$ or $|B/B_0\text{-}1.05|\leq0.015$, as listed in Table 2. The averaged data are calculated by the same methods as displayed in Figures 5b, 6b, and 7d-7i. Because the archive of TIROS-N, NOAA-06, NOAA-07, NOAA-08, NOAA-10, NOAA-12, and NOAA-14 SEM-1 data provides a constant orbital altitude, it makes >16 MeV proton fluxes fluctuate with the period about 4 months as shown in Figure 2. Therefore, as listed in the second column of Table 2, the data for recalibration of POES satellites using the SEM-1 detector will cover a longer period of time than those of POES or MetOp satellites using the SEM-2 detector. As shown in Figure 8, the data are fitted well by the black fitted curves. In Figure 8l, the black curve is from Figure 8f and the red curve is from Figure 7c. They match each other very well. Note that the nonconstant-altitude orbit location information of TIROS-N, NOAA-06, NOAA-07, NOAA-08, NOAA-10, NOAA-12, and NOAA-14 is available from https://sscweb.gsfc.nasa.gov/cgi-bin/Locator.cgi.

The traditional approach for cross calibration is to multiply counts or fluxes by constant correction factors. As shown in Figures 5d, 5e, 6d, 6e, 7a, and 7b, the ratios of >16 MeV proton fluxes or the base 10 logarithm of >16 MeV proton fluxes from NOAA-14 to those from NOAA-15 depend on L_m, B/B_0 and time. That is, each grid of (L_m, B/B_0, time) requires a correction factor for cross calibration. Therefore, the traditional approach is not advantageous for solving the problem of calibration inconsistency among POES and MetOp satellites.

Based on the fitted results listed in Table 2, >16 MeV proton fluxes from POES and MetOp satellites can be recalibrated to the standard data from one of them. We take the measurements from NOAA-15 as standard, because it has built-in accurate orbital data and the longest period of observations. Figure 9 shows the distributions of >16 MeV proton fluxes with MLT≤12:00 from POES and MetOp satellites before recalibration and after recalibration from 1978 to 2014 at the geomagnetic equator ($|B/B_0\text{-}1.0|\leq0.003$) and at magnetic field lines with $|L_m\text{-}1.20|\leq0.002$. Figure 9a displays the data of five L_m bins before recalibration on the geomagnetic equator ($|B/B_0\text{-}1.0|\leq0.003$), and Figure 9c illustrates the data of six B/B_0 bins before recalibration at
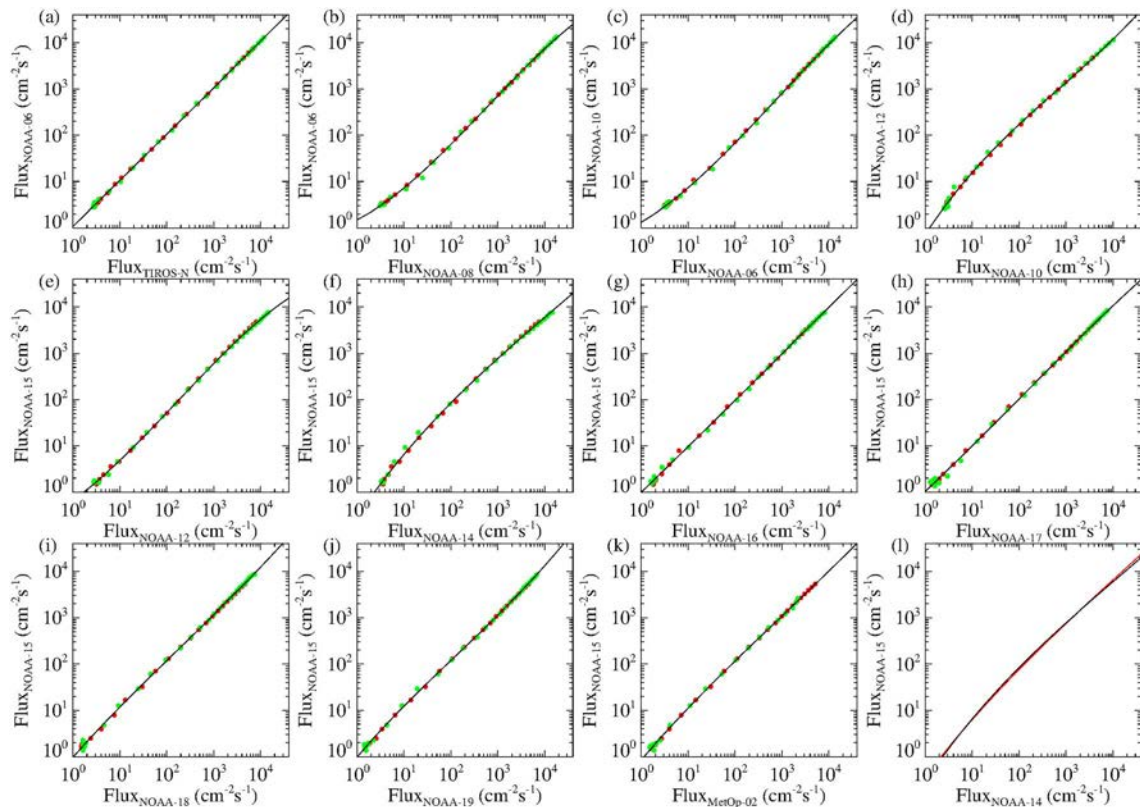
Figure 8. The fitted curves for the recalibration of >16 MeV proton fluxes among POES and MetOp satellites. The green dots are the averaged data with $|B/B_0\text{-}1.0|\leq0.003$, and the red dots are the averaged data with $|B/B_0\text{-}1.15|\leq0.02$ or $|B/B_0\text{-}1.05|\leq0.015$, as listed in Table 2. The black curves are the fitted results. In panel (l), the black curve is from panel (f) and the red curve is from Figure 7(c).

the magnetic field lines with $|L_m\text{-}1.20|\leq0.002$. Figures 9b and 9d display their recalibrated results. It is shown that the recalibrated data connect and overlap each other almost perfectly, and the measurement inconsistency among POES and MetOp satellites almost disappears.

4. Comparisons With the AP8 Model

As shown by >16 MeV proton fluxes at the geomagnetic equator in Figure 9b, the maximal and minimal fluxes are solar cycle dependent. During the period from 1979 to 2014, the maximal and minimal yearly fluxes are in 1987 and in 2002, respectively. In this section, we present the differences between the observations in these two years and the AP8 model predictions.

The AP8 model was originally developed in 1976 with data from 24 satellites from 1958 to 1970 (Fung, 1996; Sawyer & Vette, 1976). It consists of two versions, AP8 MIN and AP8 MAX. AP8 MIN and AP8 MAX are for the proton radiation belt under solar minimum and maximum conditions, respectively. They are made of maps which contain omnidirectional integral fluxes of protons in the energy range from 0.1 to 400 MeV and in the L_m range from 1.14 to 6.6. The predictions of AP8 MAX differ from those of AP8 MIN only for altitudes less than about 1000 km. The AP8 model has been developed more than 40 years. While some other proton radiation belt models were developed later, such as CRRESPRO Model, NOAAPRO Model, SAMPEX model, AP9 model (Ginet et al., 2013; Heynderickx et al., 1999; Huston & Pfitzer, 1998; Meffert & Gussenhoven, 1994), the AP8 model remains as the most widely used proton distribution model available to specify the proton radiation belt environment due to its large valid space and spectrum ranges.

In order to evaluate the AP8 model, the >16 MeV proton fluxes with MLT≤12:00 from NOAA-10 in 1987 and from NOAA-14 in 2002 are used. Figures 10a and 10b show the data of ten L_m bins with differently colored dots from NOAA-10 in 1987 and from NOAA-14 in 2002, respectively. The data do not include the lower
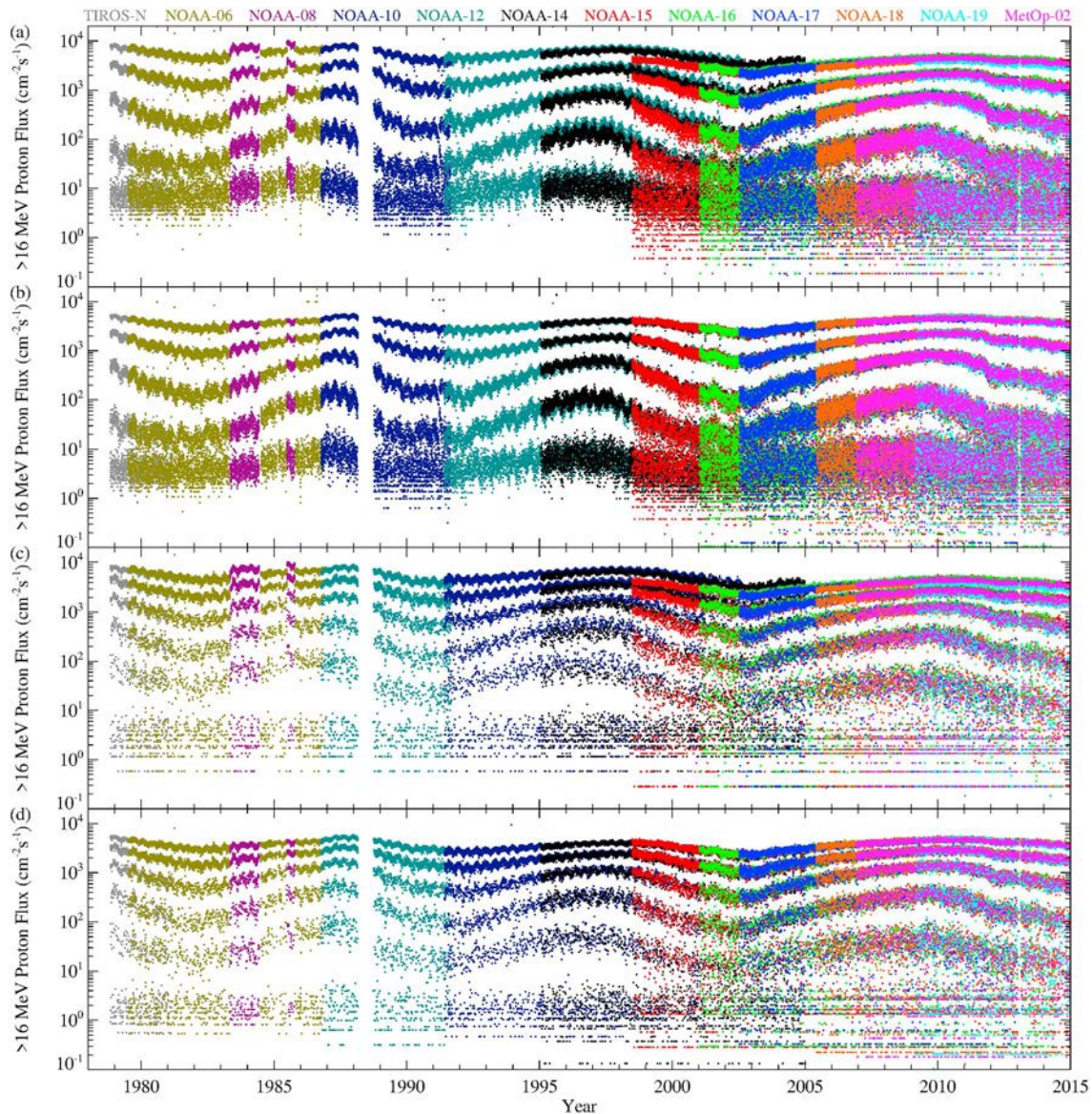
Figure 9. The distributions of >16 MeV proton fluxes with MLT≤12:00 from POES and MetOp satellites before recalibration and after recalibration from 1978 to 2014. Panel (a) shows the data of five L_m bins before recalibration with $|L_m$-1.12$|≤0.002$, $|L_m$-1.14$|≤0.002$, $|L_m$-1.16$|≤0.002$, $|L_m$-1.18$|≤0.002$, and $|L_m$-1.20$|≤0.002$ on the geomagnetic equator ($|B/B_0$-1.0$|≤0.003$), and the panel (b) displays the recalibrated results. Panel (c) illustrates the data of six B/B_0 bins before recalibration with $|B/B_0$-1.00$|≤0.001$, $|B/B_0$-1.05$|≤0.005$, $|B/B_0$-1.10$|≤0.005$, $|B/B_0$-1.15$|≤0.005$, $|B/B_0$-1.20$|≤0.005$, and $|B/B_0$-1.50$|≤0.01$ at the magnetic field lines with $|L_m$-1.20$|≤0.002$, and the panel (d) shows the recalibrated results.

branches of the bifurcations and the erroneous data, and have been recalibrated to the standard of NOAA-15 measurements. The black curves in Figures 10a and 10b are the predictions of AP8 MIN and AP8 MAX, and the black dots are the averaged values of (L_m, B/B_0) bins. From Figures 10a and 10b, it is found that there are obvious differences between the predictions from the AP8 model and the observations from NOAA-10 and NOAA-14. Figures 10c and 10d display the ratios of the averaged values of bins from NOAA-10 to the AP8 MIN predictions, and the ratios of the averaged fluxes of bins from NOAA-14 to the AP8 MAX predictions. It is demonstrated that the ratios of the observations in 1987 to the AP8 MIN predictions are within the range from 0.4 to 20, mainly from 0.5 to 3, and the ratios of the observations in 2002 to the AP8 MAX predictions are within the range from 0.06 to 10, mainly from 0.1 to 2. These ratios depend on L_m and B/B_0. When B/B_0 is larger than 1.7, the predictions of AP8 MIN and AP8 MAX are mainly larger than the observations in 1987 and in 2002, respectively. When B/B_0 is less than 1.5, the predictions of AP8 MIN are generally smaller than
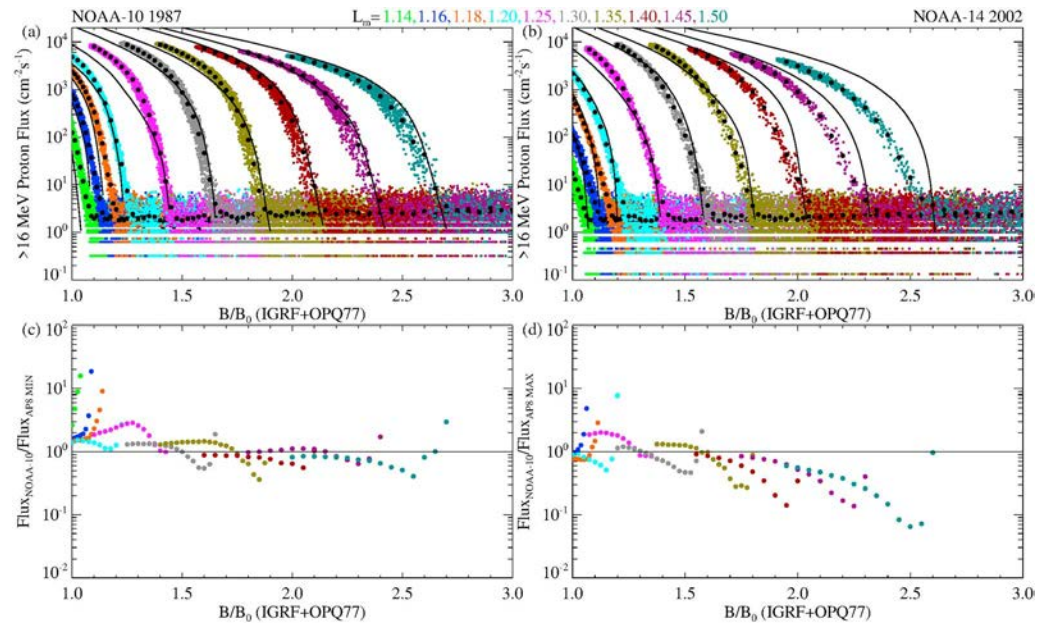
Figure 10. Comparisons of >16 MeV proton fluxes between NOAA-10 measurements in 1987 and the predictions from AP8 MIN, and between NOAA-14 measurements in 2002 and the predictions from AP8 MAX. The MLTs of data from NOAA-10 in panel (a) and from NOAA-14 in panel (b) are from 00:00 to 12:00, and these data have been recalibrated to the NOAA-15 measurements. In panels (a) and (b), the green, blue, orange, cyan, magenta, gray, olive, maroon, purple, and teal dots are the data with $|L_m\text{-}1.14|\leq0.001$, $|L_m\text{-}1.16|\leq0.001$, $|L_m\text{-}1.18|\leq0.001$, $|L_m\text{-}1.20|\leq0.001$, $|L_m\text{-}1.25|\leq0.004$, $|L_m\text{-}1.30|\leq0.005$, $|L_m\text{-}1.35|\leq0.005$, $|L_m\text{-}1.40|\leq0.005$, $|L_m\text{-}1.45|\leq0.005$, and $|L_m\text{-}1.50|\leq0.005$, and the black dots are the averaged values of $(L_m, B/B_0)$ bins. The black curves in panels (a) and (b) are the predictions of AP8 MIN and AP8 MAX, respectively. Panels (c) and (d) show the ratios of the averaged values of bins from NOAA-10 to the predictions of AP8 MIN and the ratios of the averaged values of bins from NOAA-14 to the predictions of AP8 MAX.

the observations in 1987, and the predictions of AP8 MAX are either smaller or larger than the observations in 2002.

5. Discussions

In this section, we discuss the characteristics of data bifurcation, the reasons for bifurcations, the method of cross calibration employed herein, and the reasons for the differences between the AP8 model predictions and the observations of POES and MetOp satellites.

In section 2.2, we have shown the bifurcations of >16 MeV proton fluxes from NOAA-15. There are two categories of the bifurcations in the data of >16 MeV proton fluxes. One category can distinguish the upper and lower branches by MLT and is referred to as the MLT bifurcation. The other category can distinguish the upper and lower branches by the MLAT and is referred to as the MLAT bifurcation.

After checking the data of omnidirectional protons from all channels of POES and MetOp satellites, we obtain the characteristics of the MLT bifurcation as follows: (1) for the data from NOAA POES satellites using the SEM-1, the MLT bifurcation is found in the data of >16, >36, and >80 MeV proton fluxes, the deviation of upper and lower branches varies with time, and the MLT bifurcation disappears during some periods; (2) for the data from POES satellites using the SEM-2, the MLT bifurcation is found in the data of >16, >70, and >140 MeV proton fluxes, but almost always absent in the data of >35 MeV proton fluxes. The deviation of upper and lower branches in the data of each energy channel almost does not change with time; (3) for the data from MetOp-02 using the SEM-2, the MLT bifurcation is unclear or is not found in the data of the four energy channels; and (4) the MLT bifurcation from the data of all POES satellites exists both around the geomagnetic equator and at higher latitudes.

Figure 11 shows the major characteristics of the MLT bifurcation of energetic proton data from POES and MetOp satellites. In Figure 11, the green dots are the data with MLT >12:00, and the red dots are the data
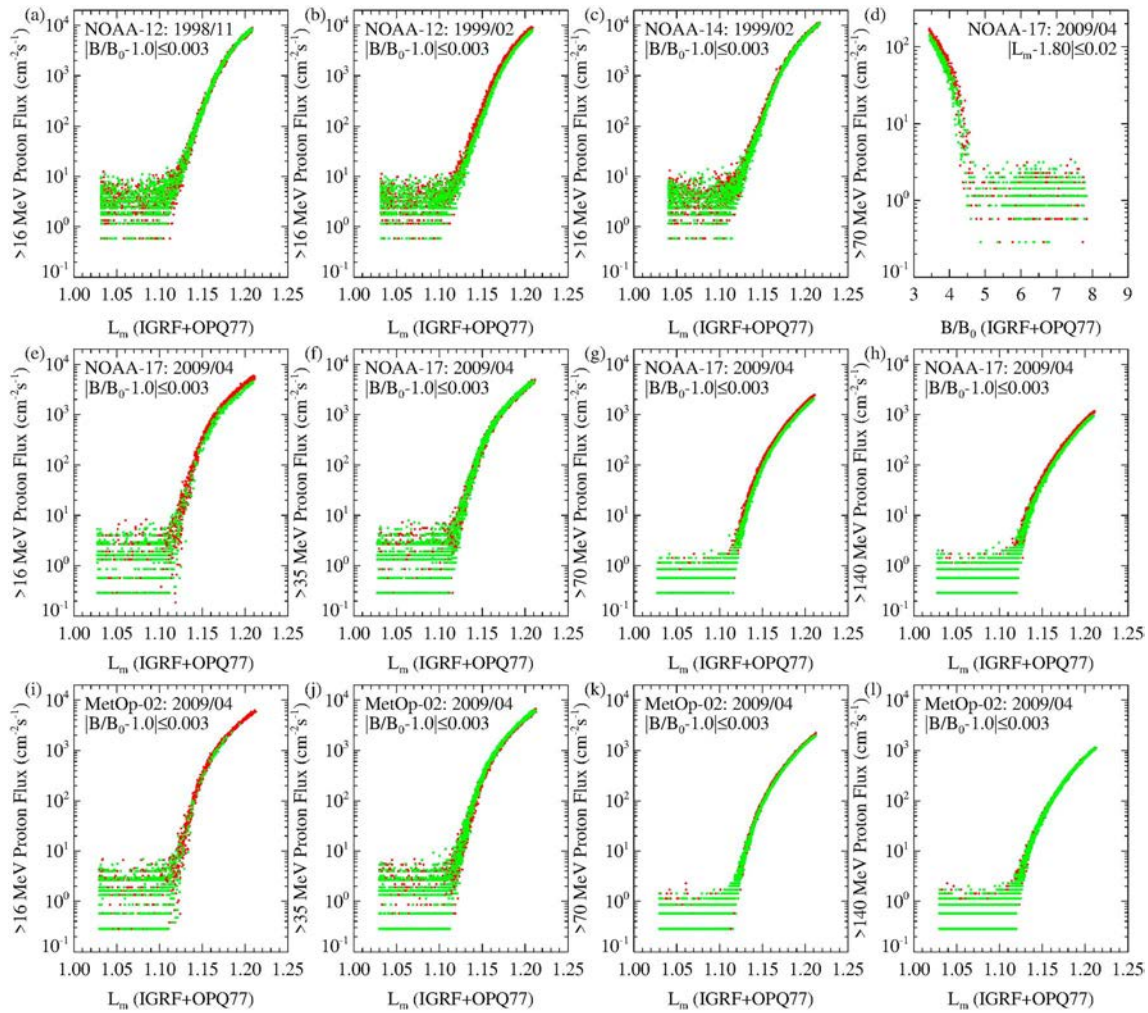
Figure 11. The MLT bifurcation of energetic proton data from POES and MetOp satellites. Panels (a)-(c) and (e)-(l) show the energetic proton fluxes (>16, >35, >70, or >140 MeV) at or near the geomagnetic equator with $|B/B_0-1.00| \leq 0.003$, and panel (d) shows >70 MeV proton fluxes at the magnetic field lines with $|L_m-1.80| \leq 0.02$. The green dots are the data with MLT $>12:00$, and the red dots are the data with MLT $\leq 12:00$. The dots in panel (a) are the data from NOAA-12 in November 1998, which have been presented in the panel, and the other panels also show the satellites and the time of the data.

with MLT $\leq 12:00$. Figures 11a and 11b display that the MLT bifurcation of >16 MeV proton fluxes with $|B/B_0-1.00| \leq 0.003$ from NOAA-12 appears in February 1999 and disappears in November 1998. However, NOAA-14 does not detect the MLT bifurcation of >16 MeV proton fluxes with $|B/B_0-1.00| \leq 0.003$ in February 1999, as shown in Figure 11c. Figures 11e-11h illustrate the data of >16, >35, >70, and >140 MeV proton fluxes with $|B/B_0-1.00| \leq 0.003$ from NOAA-17 using the SEM-2 in April 2009. It is found that the MLT bifurcation is not found in the >35 MeV proton fluxes, but exists in other energy channels. Figures 11i-11l show the data of >16, >35, >70, and >140 MeV proton fluxes with $|B/B_0-1.00| \leq 0.003$ from MetOp-02 using the SEM-2 in April 2009. The MLT bifurcation is vague or is not found in the data of four energy proton channels. Figure 11d displays the binned data of >70 MeV proton fluxes with $|L_m-1.80| \leq 0.02$ from NOAA-17 in April 2009, demonstrating that the MLT bifurcation is an equatorial and higher latitude phenomenon.

Huston and Pfitzer (1998) presented a possible reason for the MLT bifurcation. They pointed that one branch of bifurcation resulted from the northbound passes of the satellite, and the other branch resulted from the southbound passes of the satellite. They claimed that it is due to an ephemeris timing error and that the bifurcation can be eliminated by the time shift of the satellite ephemeris. However, as shown in Figure 11, the MLT bifurcation is not present in the data of all energetic proton channels. If we shift the time of NOAA-17 ephemeris, the MLT bifurcation of >16 MeV proton fluxes can be eliminated, but the MLT
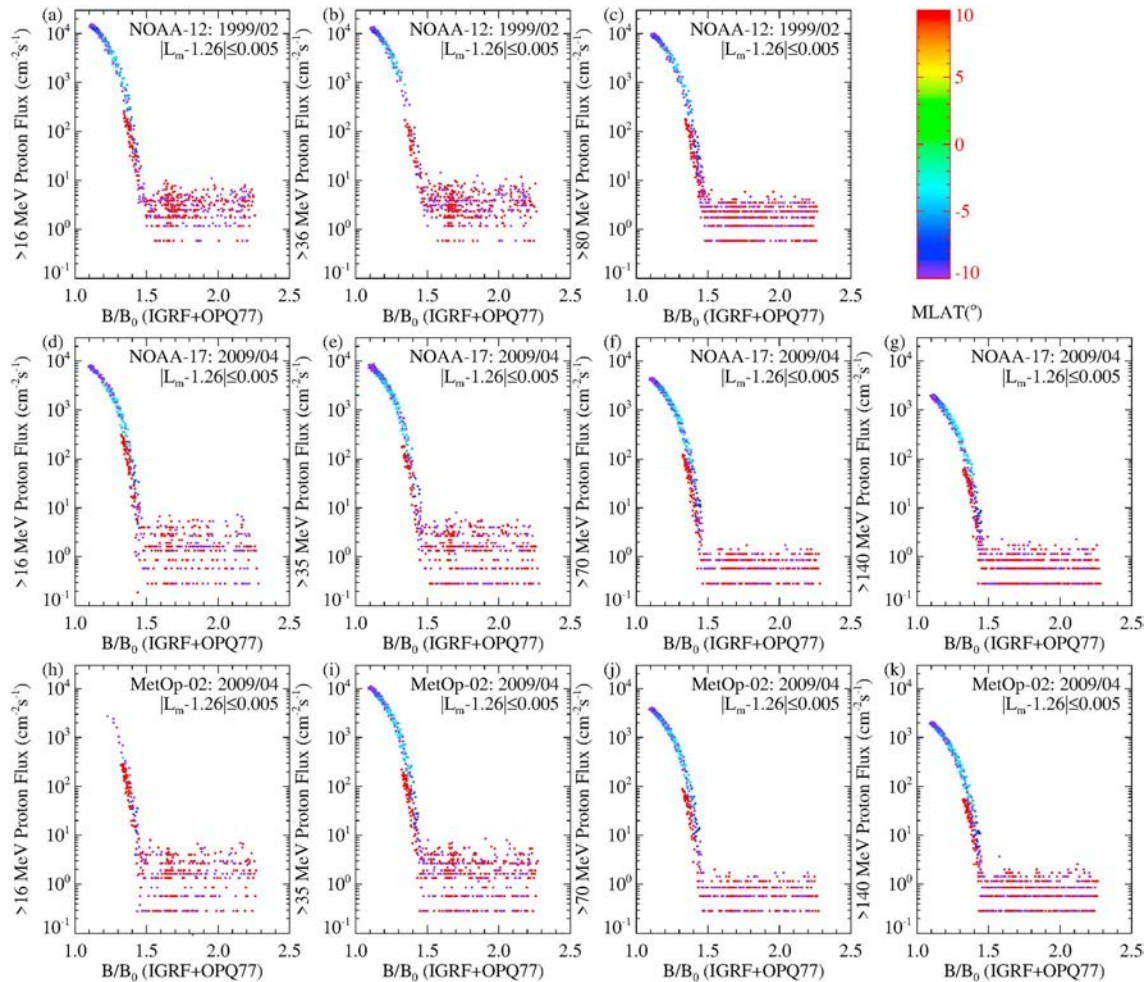
Figure 12. The MLAT bifurcation of energetic proton data with MLT≤12:00 from POES and MetOp satellites. The color dots in the panels (a)-(c) show >16 MeV, >36 MeV, and >80 MeV proton fluxes with $|L_m$-1.26$|$≤0.005 from NOAA-12 in February 1999, respectively. The color dots in the panels (d)-(k) show >16, >35, >70, and >140 MeV proton fluxes with $|L_m$-1.26$|$≤0.005 from NOAA-17 and MetOp-02 in April 2009. The color of dots represents the values of magnetic latitude corresponding to the top-right color bar.

bifurcation of >35 MeV proton fluxes will appear. Therefore, the ephemeris timing error argument cannot be used to interpret the MLT bifurcation, at least for newer satellites.

The MLT bifurcation is also unlikely from the MLT asymmetry of the proton radiation belt. As shown in Figure 2c, NOAA-15 and NOAA-16 have same MLT in late 2008, and their MLTs are different in other periods from 2001 to 2014. After recalibration, the distributions of >16 MeV proton fluxes with MLT≤12:00 from NOAA-15 and NOAA-16 satellites are well consistent from 2001 to 2014 in Figures 9b and 9d. That is to say, the MLT asymmetry of the proton radiation belt is not seen. Figure 2c shows that the MLTs of the data with $|B/B_0$-1.00$|$≤0.003 from MetOp-02 and from NOAA-17 are the same in April 2009. Figure 11 shows that the MLT bifurcation is observed by NOAA-17 in >16, >70, and >140 MeV proton channels, but not observed by MetOp-02. It indicates that there are other reasons for the MLT bifurcation.

In the regions with same L_m and B/B_0 but different MLT, the directions of the omnidirectional proton detector may be different. The calculation of omnidirectional integral fluxes by assuming the isotropic pitch angle distribution may cause the MLT bifurcation for the data from the omnidirectional proton detectors with the 120° full-opening view angle, because the pitch angle distribution of energetic protons is anisotropic. It is unlikely the main reason for the MLT bifurcation, because the MLT bifurcation is almost always absent in the data of >35 MeV proton fluxes from POES satellites using the SEM-2.
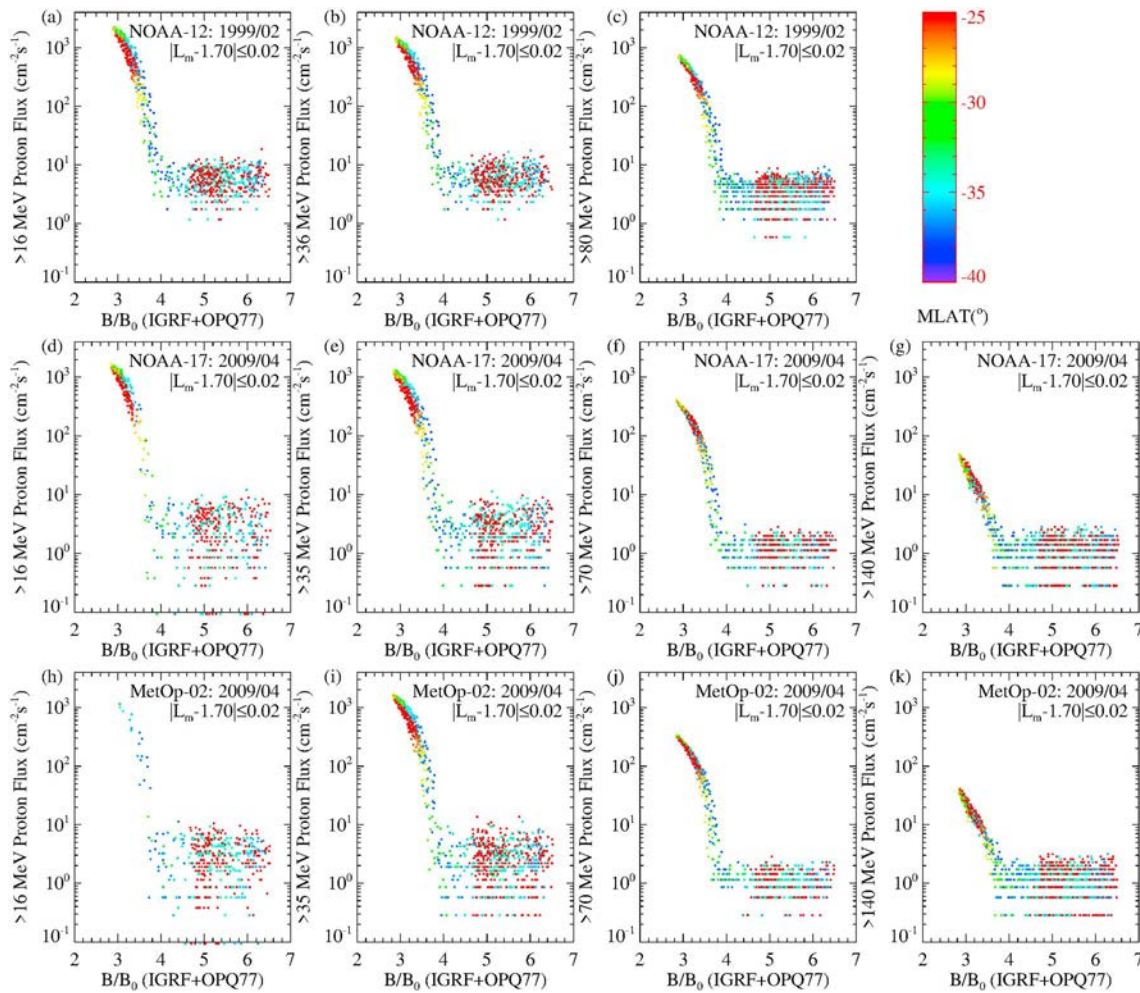
Figure 13. The MLAT bifurcation of energetic proton data with MLT>12:00 from POES and MetOp satellites. The format is as Figure 12, but the data are in the regions with $|L_m-1.70|\leq0.02$.

The main reason for the MLT bifurcation may be due to the direction of MEPED package. The POES satellites from NOAA-15 to NOAA-19 and the MetOp-02 satellite were equipped with same MEPED package of SEM-2. However, the directions of these satellites' MEPED are different. The central axis of the MEPED package on POES satellites is rotated twice: 9° off the –X direction, and an additional 9.08° off the +Y direction, but the MEPED package on MetOp-02 satellite has no rotations (Green, 2013a). This is likely the main reason that the omnidirectional proton detectors of POES satellites obtain the MLT bifurcation, but those of MetOp-02 satellite don't.

For the SEM-2 from NOAA15 to NOAA-19, the central axis of each omnidirectional detector is not parallel to the X axis, which points earthward, so the east-west effect in the observations should be considered for the MLT bifurcation. At the point of observation, the proton traveling toward the east has guiding centers at higher altitudes than those traveling toward the west. Due to the diminution of atmospheric density with altitude, the eastward flux is expected to be larger than the westward flux (Heckman & Nakano, 1963; Lenchek & Singer, 1962). If the MLT bifurcation is due to the east-west effect, it should exist in other proton channels. The MLT bifurcation is found in the data of >16, >70, and >140 MeV proton fluxes, but it is almost always absent in the data of >35 MeV proton fluxes, as shown in Figures 11e-11h. Why the direction of MEPED package causes the MLT bifurcation and why the channel of >35 MeV proton from POES satellites using the SEM-2 is not influenced, quite possibly depend on the satellite's specific structure. The variation of the actual orbital altitudes of TIROS-N to NOAA-14 satellites can be the reason justifying that the deviation of upper and lower branches varies with time.
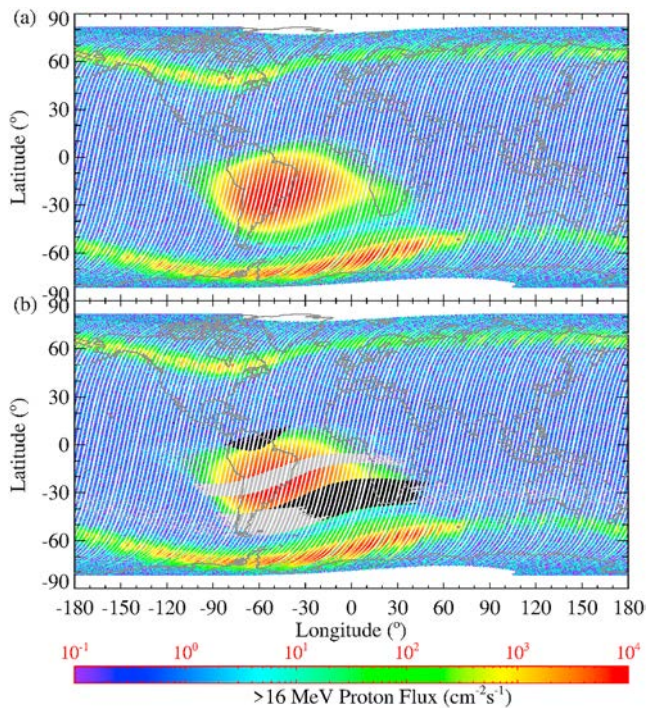
Figure 14. The distribution of >16 MeV proton fluxes with MLT≤12:00 and the distribution of lower and upper branches of MLAT bifurcation from NOAA 12 in January 1991. The color dots in panels (a) and (b) are the data with MLT≤12:00, and their colors represent the values of >16 MeV proton fluxes corresponding to the bottom color bar. In panel (b), the black dots in the SAA are the data of the lower branches of the MLAT bifurcation, and the gray dots in the SAA are the data of the upper branches of the MLAT bifurcation.

There are two types of MLAT bifurcation. The first type, similar to that shown in Figure 3e, appears in the region $1.22 \leq L_m \leq 1.31$. The B/B_0 area of the lower branch is clearly smaller than that of the upper branch. This type of MLAT bifurcation exists in all energetic proton channels from POES and MetOp satellites. Figure 12 shows the distribution of energetic proton data with $|L_m\text{-}1.26| \leq 0.005$ and MLT≤12:00 from NOAA-12, NOAA-17, and MetOp-02. It shows that this type of MLAT bifurcation apparently exists for all energetic proton channels.

The other type of MLAT bifurcation, similar to that shown in Figure 3f, appears in the region $1.54 \leq L_m \leq 2.20$. The B/B_0 area of the lower branch is similar to that of the upper branch. The deviation of upper and lower branches is related to the proton energy. For the >16, >35, and >36 MeV proton channels from POES and MetOp satellites, this type of MLAT bifurcation is clear, while it is unclear for the >70 and >80 MeV proton channels and disappears for the >140 MeV proton channel. Figure 13 shows the distribution of energetic proton data with $|L_m\text{-}1.70| \leq 0.02$ and MLT>12:00 from NOAA-12, NOAA-17, and MetOp-02. It apparently demonstrates the above characteristics of this type of MLAT bifurcation. Note that >16 MeV proton fluxes with $1.54 \leq L_m \leq 2.20$ and MLT≤12:00 lack good coverage of the lower branches and therefore we use the data with MLT>12:00.

Figure 14 shows the distribution of >16 MeV proton fluxes with MLT≤12:00 and the distribution of lower and upper branches of MLAT bifurcation from NOAA 12 in January 1991 in latitude-longitude coordinates. Figure 14a illustrates the data coverage of the whole SAA in the proton radiation belt over the longitude-latitude map. In Figure 14b, the lower (black dots) and upper (gray dots) branches of the first type MLAT bifurcation are in the north of SAA and in the central strip of SAA, respectively. The lower (black dots) and upper (gray dots) branches of the second type MLAT bifurcation are in the south of SAA at different longitudes.

For the bifurcation as shown in Figure 12, the errors of the geomagnetic field model for calculating B, B_0 and L_m can cause the MLAT bifurcation in the data of all energetic proton channels.

For the MLAT bifurcation as shown in Figure 13, it mainly appears in the >16, >35, and >36 MeV proton channels away from the geomagnetic equator. This type of MLAT bifurcation is probably related to the full-opening view angle of detectors and the anisotropic pitch angle distribution of proton radiation belt. In section 2.1, we calculate the omnidirectional integral fluxes by assuming the isotropic pitch angle distribution, but the pitch angle distribution of energetic protons is actually anisotropic. For the >70 MeV and >140 MeV proton channels of SEM-2, their full-opening view angles are 180°, covering the hemisphere, so the omnidirectional integral fluxes are not influenced by the assumption of the isotropic pitch angle distribution, and this type of MLAT bifurcation is not clear, or not present in the >70 and >140 MeV proton channels. However, for the >16 and >35 MeV proton channels of SEM-2, and the >16 and >36 MeV proton channels of SEM-1, their full-opening view angles are only 120°. Each detector may have the different coverage of pitch angles corresponding to detector's view angle at the same L_m and B/B_0 with different MLATs, so the assumption of isotropic pitch angle distribution will cause the errors for calculating omnidirectional integral fluxes. For the >80 MeV proton channel of SEM-1, its full-opening view angle is also 120°, but this type of MLAT bifurcation is not obvious. It may be related to the anisotropic degree of pitch angle distribution of >80 MeV proton.

In order to confirm the dominant reasons responsible for above bifurcations, more reliable data are required to do simulations, such as the geomagnetic field, the information on satellite's structure and equipment, the energy spectrum distribution and pitch angle distribution of radiation belt protons and electrons, and so on.

Figure 9 shows that the calibration inconsistency of >16 MeV proton fluxes is not very clear in the data from POES satellites using the SEM-1 and vague in the data from POES satellites using the SEM-2. However, the calibration inconsistency between SEM-1 and SEM-2 measurements is obvious due to different instrument designs, accommodations, and characteristics. In order to remove or decrease the inconsistency of >16 MeV proton fluxes among the POES and MetOp satellites measurements, a third-degree polynomial function is used to do the cross calibration among the POES and MetOp satellites' measurements. This method of the cross calibration is equivalent to the adjustments of the conversion tables of POES and MetOp satellites in counting the energetic protons.

According to the data of >16 MeV proton fluxes at the geomagnetic equator from 1979 to 2014, the maximal and minimal yearly fluxes are in 1987 and in 2002, respectively. AP8 MIN gives the distribution of the proton radiation belt in the solar minimum of 1964, and AP8 MAX gives the distribution of the proton radiation belt in the solar maximum of 1970. By comparisons with the observations in 1987 and in 2002, the ratios of the observations in 1987 to the predictions of AP8 MIN are within the range mainly from 0.5 to 3, and the ratios of the observations in 2002 to the predictions of AP8 MAX are within the range mainly from 0.1 to 2. The ratios depend on the L_m and B/B_0. The differences between the AP8 model predictions and the observations from POES satellites are mainly due to the long-term variations of the proton radiation belt in the SAA, as shown in Figures 9b and 9d. During different solar cycles, the distributions of the maximal and minimal yearly proton fluxes are different. In addition, there are other reasons accounting for these differences, for example, the different calibration between the data for the AP8 model and the observations from POES satellites, the different geomagnetic field models used for calculating B, B_0 and L_m, the errors of data for the AP8 model, and the errors of observations from POES satellites.

6. Conclusions

In this study we have comprehensively investigated the >16 MeV proton omnidirectional integral fluxes from the SEM-1 onboard the TIROS-N, NOAA-06, NOAA-07, NOAA-08, NOAA-10, NOAA-12, and NOAA-14 and from the SEM-2 onboard the NOAA-15, NOAA-16, NOAA-17, NOAA-18, NOAA-19, and MetOp-02. The data with an 8-s resolution cover the period from 1978 to 2014, about 3.5 solar cycles. It is found that the calibration inconsistency among POES and MetOp satellites, the data bifurcations, and the erroneous data actually exist in the data of >16 MeV proton fluxes.

There are two categories of the bifurcations in the data of >16 MeV proton fluxes. One of the bifurcations can clearly separate the upper and lower branches by MLT, abbreviated as the MLT bifurcation, and the other bifurcation can clearly separate the upper and lower branches by MLAT, abbreviated as the MLAT bifurcation. The MLT and MLAT bifurcations also appear in the data of protons with other energies. The MLT bifurcation is possibly due to the direction of MEPED package. The MLAT bifurcation includes two types. The lower branch of one type of the MLAT bifurcation is in the north of SAA, possibly due to the errors of the geomagnetic field model. The other type of the MLAT bifurcation is in the south of SAA, probably related to the full-opening view angle of the detectors and the anisotropic pitch angle distribution of proton radiation belt.

For the calibration inconsistency of >16 MeV proton fluxes among POES and MetOp satellites, a third-degree polynomial function is fitted for cross calibration. We have proved that the curve of the fitted function for every two POES and MetOp satellites is almost independent of L_m, B/B_0, and time in the valid range. The coefficient values of the fitted function for every two satellites are presented. Based on these fitted functions, the data of >16 MeV proton fluxes with MLT≤12:00 from POES and MetOp satellites, after the lower branches of bifurcations and the erroneous data are removed, can be recalibrated to a standard (i.e., NOAA-15 in this study) to ensure the measurement consistency among different satellites.

Based on the recalibrated data of >16 MeV proton fluxes with MLT≤12:00 at the geomagnetic equator from 1979 to 2014, it is found that the maximal and minimal yearly proton fluxes are in 1987 and in 2002. By comparisons with the observations in 1987 and in 2002, the ratios of the observations in 1987 to the AP8 MIN predictions are within the range mainly from 0.5 to 3, and the ratios of the observations in 2002 to the AP8 MAX predictions are within the range mainly from 0.1 to 2. These ratios depend on L_m and B/B_0. The differences between the predictions of the AP8 model and the observations from POES satellites are

mainly due to the long-term variations of the proton radiation belt in the SAA. Note that the distributions of the maximal and minimal yearly proton fluxes are different in different solar cycles.

With the method of cross calibration presented in this paper, the data of other energetic proton channels can also be recalibrated to a carefully selected standard to ensure measurement consistency among different satellites. Based on the recalibrated data of >16 MeV proton fluxes from 1978 to 2014, the characteristics of long-term variations of the proton radiation belt in the SAA can be investigated in detail and an improved model of the proton radiation belt can be pursued, which is left as our future investigation.

References

Albert, J. M., Ginet, G. P., & Gussenhoven, M. S. (1998). CRRES observations of radiation belt protons: 1. Data overview and steady state radial diffusion. *Journal of Geophysical Research*, *103*(A5), 9261–9273. https://doi.org/10.1029/97JA02869

Asikainen, T., & Mursula, K. (2011). Recalibration of the long-term NOAA/MEPED energetic proton measurements. *Journal of Atmospheric and Solar - Terrestrial Physics*, *73*(2-3), 335–347. https://doi.org/10.1016/j.jastp.2009.12.011

Asikainen, T., Mursula, K., & Maliniemi, V. (2012). Correction of detector noise and recalibration of NOAA/MEPED energetic proton fluxes. *Journal of Geophysical Research*, *117*, A09204. https://doi.org/10.1029/2012JA017593

Badhwar, G. D. (1997). Drift rate of the South Atlantic Anomaly. *Journal of Geophysical Research*, *102*(A2), 2343–2349. https://doi.org/10.1029/96JA03494

Berger, T. (2008). Radiation dosimetry onboard the International Space Station ISS. *Zeitschrift für Medizinische Physik*, *18*(4), 265–275. https://doi.org/10.1016/j.zemedi.2008.06.014

Blake, J. B., Kolasinski, W. A., Fillius, R. W., & Mullen, E. G. (1992). Injection of electrons and protons with energies of tens of MeV into L < 3 on 24 March 1991. *Geophysical Research Letters*, *19*(8), 821–824. https://doi.org/10.1029/92GL00624

Bourdarie, S., Blake, B., Cao, J. B., Friedel, R., Miyoshi, Y., Panasyuk, M., & Underwood, C. (2008). Data analysis procedure, COSPAR, Panel on Radiation Belt Environment Modeling, V1.2.

Croley, D. R. Jr., Schulz, M., & Blake, J. B. (1976). Radial diffusion of inner-zone protons: Observations and variational analysis. *Journal of Geophysical Research*, *81*(4), 585–594. https://doi.org/10.1029/JA081i004p00585

Dragt, A. J., Austin, M. M., & White, R. S. (1966). Cosmic ray and solar proton albedo neutron decay injection. *Journal of Geophysical Research*, *71*(5), 1293–1304. https://doi.org/10.1029/JZ071i005p01293

Duzellier, S. (2005). Radiation effects on electronic devices in space. *Aerospace Science and Technology*, *9*(1), 93–99. https://doi.org/10.1016/j.ast.2004.08.006

Evans, D. S., & Greer, M. S. (2006). *Polar Orbiting Environmental Satellite Space Environment Monitor–2 Instrument descriptions and archive data documentation*, *NOAA Tech. Mem. 1.4*, (). Boulder, Colorado: Space Environ. Lab.

Farley, T. A., Tomassian, A. D., & Walt, M. (1970). Source of high-energy protons in the Van Allen radiation belt. *Physical Review Letters*, *25*(1), 47–49. https://doi.org/10.1103/PhysRevLett.25.47

Freden, S. C., & White, R. S. (1962). Trapped proton and cosmic-ray albedo neutron fluxes. *Journal of Geophysical Research*, *67*(1), 25–29. https://doi.org/10.1029/JZ067i001p00025

Fung, S. F. (1996). Recent development in the NASA trapped radiation models. In *Radiation Belts: Models and Standards*. Washington, D. C: American Geophysical Union. https://doi.org/10.1029/GM097p0079

Galand, M., & Evans, D. (2000). Radiation damage of the proton MEPED detector on POES (TIROS/NOAA) satellites. NOAA Technical Memorandum, Boulder, Colorado OAR 456-SEC 42.

Ginet, G. P., O'Brien, T. P., Huston, S. L., Johnston, W. R., Guild, T. B., Friedel, R., et al. (2013). AE9, AP9 and SPM: New models for specifying the trapped energetic particle and space plasma environment. *Space Science Reviews*, *179*(1-4), 579–615. https://doi.org/10.1007/s11214-013-9964-y

Green, J. C. (2013a). MEPED telescope data processing algorithm theoretical basis document Version 1.0, 77pp., *NOAA National NESDIS-NGDC*.

Green, J. C. (2013b). TED data processing algorithm theoretical basis document, version 1.0, 81 pp., NOAA National Geophysical Data Center.

Green, J. C. (2013c), External users manual POES/MetOp SEM-2 processing, 20pp., NOAA National Geophysical Data Center document.

Heckman, H. H., & Nakano, G. H. (1963). East-west asymmetry in the flux of mirroring geomagnetically trapped protons. *Journal of Geophysical Research*, *68*(8), 2117–2120. https://doi.org/10.1029/JZ068i008p02117

Heynderickx, D., Kruglanski, M., Pierrard, V., Lemaire, J., Looper, M. D., & Blake, J. B. (1999). A low altitude trapped proton model for solar minimum conditions based on SAMPEX/PET data. *IEEE Transactions on Nuclear Science*, *46*(6), 1475–1480. https://doi.org/10.1109/23.819110

Huston, S. L., & Pfitzer, K. A. (1998). Space environment effects: Low-altitude trapped radiation model, NASA/CR-1998-208593, NASA Marshall Space Flight Center.

Jentsch, V. (1981). On the role of external and internal source in generating energy and pitch angle distributions of inner-zone protons. *Journal of Geophysical Research*, *86*(A2), 701–710. https://doi.org/10.1029/JA086iA02p00701

Lenchek, A. M., & Singer, S. F. (1962). Effects of finite gyroradii of geomagnetically trapped protons. *Journal of Geophysical Research*, *67*(10), 4073–4075. https://doi.org/10.1029/JZ067i010p04073

Machol, J. (2012). POES/MetOp SEM-2 omni flux algorithm theory and software description, version 1.0, 43pp., NOAA National Geophysical Data Center document.

McIlwain, C. E. (1961). Coordinates for mapping the distribution of magnetically trapped particles. *Journal of Geophysical Research*, *66*(11), 3681–3691. https://doi.org/10.1029/JZ066i011p03681

Meffert, J. D., & Gussenhoven, M. S. (1994). CRRESPRO documentation, *Technical Report*, PL-TR-94-2218, Phillips Laboratory, AFMC, Hanscom AFB, MA.

Miroshnichenko, L. I. (2003). *Radiation hazard in space*. Dordrecht: Kluwer Academic Publishers. ISBN:1402015380

Ni, B., Li, W., Thorne, R. M., Bortnik, J., Green, J., Kletzing, C., et al. (2014). A novel technique to construct the global distribution of whistler-mode chorus wave intensity using low-altitude POES electron data. *Journal of Geophysical Research: Space Physics*, *119*, 5685–5699. https://doi.org/10.1002/2014JA019935

Ødegaard, L.-K. G. (2013). *Recalibration of the MEPED proton detectors onboard NOAA POES satellites*, Master thesis in Space Physics, Department of Physics and Technology,. Norway: University of Bergen.

Olson, W. P., & Pfitzer, K. A. (1977). Magnetospheric magnetic field modeling, Annual Scientific Report, AFOSR Contract No. F44620-75-C-0033.

Qin, M., Zhang, X., Ni, B., Song, H., Zou, H., & Sun, Y. (2014). Solar cycle variations of trapped proton flux in the inner radiation belt. *Journal of Geophysical Research: Space Physics*, *119*, 9658–9669. https://doi.org/10.1002/2014JA020300

Raben, V. J., Evans, D. S., Sauer, H. H., Sahm, S. R., & Huynh, M. (1995). TIROS/NOAA satellite space environment monitor data archive document: 1995 update, NOAA Technical Memorandum, ERL SEL-86, Boulder, Colorado.

Redmon, R. J., Rodriguez, J. V., Gliniak, C., & Denig, W. F. (2017). Internal charge estimates for satellites in low Earth orbit and space environment attribution. *IEEE Transactions on Plasma Science*, *45*(8), 1985–1997. https://doi.org/10.1109/TPS.2017.2656465

Samwel, S. W., Hady, A. A., Mikhail, J. S., Ibrahim, M. & Hanna, Y. S. (2008). Studying the total ionizing dose and displacement damage dose effects for various orbital trajectories, First Middle East and Africa IAU-Regional Meeting Proceedings MEARIM, No. 1, https://doi.org/10.10107/977403330200044

Sandanger, M. I., Ødegaard, L.-K. G., Nesse Tyssøy, H., Stadsnes, J., Søraas, F., Oksavik, K., & Aarsnes, K. (2015). In-flight calibration of NOAA POES proton detectors—Derivation of the MEPED correction factors. *Journal of Geophysical Research: Space Physics*, *120*, 9578–9593. https://doi.org/10.1002/2015JA021388

Sawyer, D. M., & Vette, J. I. (1976). AP-8 trapped proton environment for solar maximum and solar minimum, NASA STI/Recon Technical Report, N77:18983

Selesnick, R. S., Baker, D. N., Jaynes, A. N., Li, X., Kanekal, S. G., Hudson, M. K., & Kress, B. T. (2014). Observations of the inner radiation belt: CRAND and trapped solar protons. *Journal of Geophysical Research: Space Physics*, *119*, 6541–6552. https://doi.org/10.1002/2014JA020188

Selesnick, R. S., Hudson, M. K., & Kress, B. T. (2010). Injection and loss of inner radiation belt protons during solar proton events and magnetic storms. *Journal of Geophysical Research*, *115*, A08211. https://doi.org/10.1029/2010JA015247

Selesnick, R. S., Looper, M. D., & Mewaldt, R. A. (2007). A theoretical model of the inner proton radiation belt. *Space Weather*, *5*, S04003. https://doi.org/10.1029/2006SW000275

Shao, X., Papadopoulos, K., & Sharma, A. S. (2009). Control of the energetic proton flux in the inner radiation belt by artificial means. *Journal of Geophysical Research*, *114*, A07214. https://doi.org/10.1029/2009JA014066

Singer, S. F. (1958). Radiation belt and trapped cosmic-ray albedo. *Physical Review Letters*, *1*(5), 171–173. https://doi.org/10.1103/PhysRevLett.1.171

Thébault, E., Finlay, C. C., Beggan, C. D., Alken, P., Aubert, J., Barrois, O., et al. (2015). International Geomagnetic Reference Field: the 12th generation. *Earth, Planets and Space*, *67*(1). https://doi.org/10.1186/s40623-015-0228-9

Yando, K., Millan, R. M., Green, J. C., & Evans, D. S. (2011). A Monte Carlo simulation of the NOAA POES Medium Energy Proton and Electron Detector instrument. *Journal of Geophysical Research*, *116*, A10231. https://doi.org/10.1029/2011JA016671